Chem Soc Rev

Crucial Breakthrough of Second Near-infrared Biological Window Fluorophores: Design and Synthesis toward Multimodal Imaging and Theranostics

Journal:	*Chemical Society Reviews*
Manuscript ID	CS-TRV-03-2018-000234
Article Type:	Tutorial Review
Date Submitted by the Author:	28-Mar-2018

Complete List of Authors:	He, Shuqing; Stanford University Department of Radiology, 1201 Welch Rd. Lucas P095 Stanford, CA, USA 94305 650-723-7866; Shenzhen University, Key Laboratory of Optoelectronic Devices and Systems of Ministry of Education and Guangdong Province, College of Optoelectronic Engineering, Shenzhen University, Shenzhen 518060, P. R. China Song, Jun; Shenzhen University, Institute of Optoelectronics Qu, Junle; Shenzhen University, Institute of Optoelectronics Cheng, Zhen; Stanford University, Department of Radiology

TUTORIAL REVIEW

Submission to:

Chemical Society Reviews

Crucial Breakthrough of Second Near-infrared Biological Window Fluorophores: Design and Synthesis toward Multimodal Imaging and Theranostics

Shuqing He,[a,b] Jun Song,*[a] Junle Qu,*[a] and Zhen Cheng*[b]

* To whom correspondence should be addressed.

[a] Key Laboratory of Optoelectronic Devices and Systems of Ministry of Education and Guangdong Province, College of Optoelectronic Engineering, Shenzhen University, Shenzhen 518060, P. R. China
E-mail: songjun@szu.edu.cn; jlqu@szu.edu.cn

[b] Molecular Imaging Program at Stanford (MIPS), Bio-X Program, and Department of Radiology, Canary Center at Stanford for Cancer Early Detection, Stanford University, Stanford, California 94305-5344, USA
E-mail: zcheng@stanford.edu

Abstract

Development of fluorophores and molecular probes for the second near-infrared biological window (NIR-II, 1000–1700 nm) represents an important, new rising and dynamic field in molecular imaging, chemical biology and materials chemistry. Because of reduced scattering, minimal absorption and negligible autofluorescence, NIR-II imaging provides high resolution, high signal-to-noise ratio, and deep tissue penetration capability. Among various state-of-the-art bioimaging modalities, one of the greatest challenges in developing novel probes is to achieve both high resolution and sensitivity. The chemical design and synthesis of NIR-II fluorophores suitable for multimodal imaging is thus emerging as a new and powerful strategy to realize high definition images. NIR-II Fluorophores may convert NIR-II photons into heat for photothermal therapy and be excited by NIR-II light to produce singlet oxygen for photodynamic therapy. The presence of simultaneous diagnostic and therapeutic capabilities in a single probe can be used for precise treatment. In this review, we focus on recent advances in the chemical design and synthesis of NIR-II fluorophores, from small organic molecules to organic and inorganic nanoparticles, and we further discuss the recent advancements and key operating differences in the reported NIR-II imaging systems and NIR-II imaging based biomedical applications such as multimodal imaging, photothermal and photodynamic therapy, guidance for intraoperative surgery, and drug delivery.

Key learning points

(1) Recent advances in chemical strategies to design and synthesize NIR-II fluorophores
(2) The power of chemical architecture in NIR-II probes for multimodal imaging techniques
(3) Analysis, at the cellular level, using structure-function relationships between NIR-II probes and biological systems
(4) Diversity-oriented NIR-II fluorophores as an alternative to conventional rational design in theranostics
(5) Perspectives and challenges of application of NIR-II fluorophores

1. Introduction

Fluorescence imaging does not require ionizing radiation and can be developed as non-invasive or the minimally invasive techniques. It can be conveniently used for the exploration of biological phenomena, importantly, allowing real-time acquisition of wide-field images with high signal-to-noise ratio and excellent spatial and temporal resolution. Key issues in fluorescence imaging include autofluorescence, quenching, photobleaching and low depth of tissue penetration. Compared with fluorescence imaging in the visible spectrum (400–700 nm), fluorescent imaging in near infrared (NIR) window (700–1700 nm) offers considerable advantages in terms of reduced photon scattering, lower absorption and minimal interference from autofluorescence (Scheme 1). NIR imaging allows high resolution and signal-to-noise ratio and has tremendous potential in molecular diagnostic and therapeutic applications.[1]

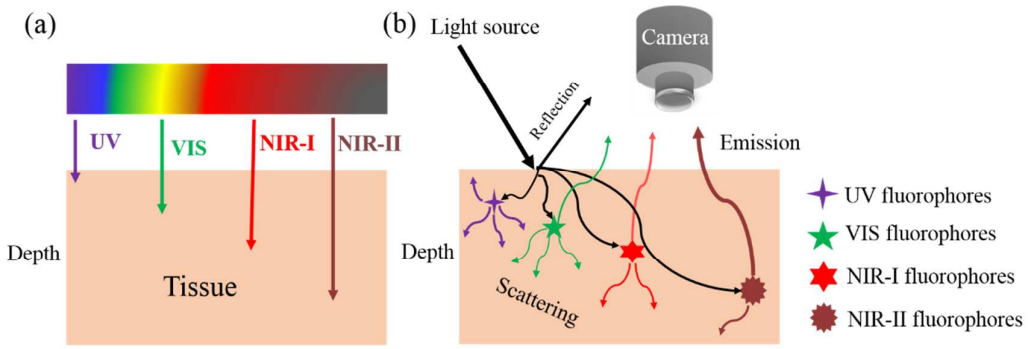

Scheme 1. Schematic illustrations. (a) Tissue penetration depth of light with different wavelengths. (b) Light when entering a tissue can be reflected and absorbed by molecules within the tissue or excite fluorophores to emit light at a different wavelength. The NIR-II fluorophores show the lowest scattering and deepest penetration depth compared with UV/VIS and NIR-I fluorophores.

Over the past decade, fluorescence imaging in the first NIR window (NIR-I, 700–900 nm) has been widely studied in fundamental research, preclinical and clinical applications, partly because of the readily availability of wide range of fluorophores, such as indocyanine green (ICG, λ_{ex}= 808 nm, λ_{em} = 822 nm) and methylene blue (MB, λ_{ex} = 665 nm, λ_{em} = 686 nm), which have been approved by the Food and Drug Administration (FDA) for clinical use. NIR-II biological window is broadly defined as wavelengths in the range 1000–1700 nm. Smaller optical sub-windows such as the NIR-IIa (1300–1400 nm) and the NIR-IIb (1500–1700 nm) have obtained further improvements in fluorescence imaging metrics. The 1400–1500 nm window is typically avoided due to the presence of a water overtone absorbance peak. The NIR-II fluorescence imaging can provide even higher signal-to-noise ratio (because of lower tissue autofluorescence) and deeper tissue penetration (because of lower signal attenuation)[2] (Fig. 1). NIR-II imaging is also able to provide micron-scale resolution, which is very difficult to achieve by NIR-I and many other imaging modalities such as positron emission tomography (PET) and single photon emission computed tomography (SPECT).

Because NIR-II fluorescence imaging is a new rising field, only very recently fluorophores with emission at suitable wavelengths have been explored. The poor water solubility, low photostability, low quantum yield, and scarce molecules with suitable NIR-II bandgaps have further limited the applications and development of NIR-II imaging technique. Interestingly in the last couple of years, a series of organic small molecules, and organic and inorganic nanomaterials, with precisely controlled structures and intrinsic near infrared emission in NIR-II window, have been developed to allow the acquisition of high definition NIR-II images at wavelengths well above 1000 nm.

One of the greatest challenges in bioimaging is to achieve both high resolution and contrast. Despite huge advances in NIR-II fluorescence imaging for preclinical applications, the whole information at different spatial scales and resolutions is not likely to be obtained using a single imaging modality. Multimodal imaging, which combines two or more imaging modalities, has emerged as a strategy to address this

challenge. Together with the advances in imaging techniques, it is critical to create complementary imaging contrast agents. They should enhance the sensitivity to reveal physiological structure and specific molecular information of diseases. In diagnostic imaging, however, modality selection is driven by the fact that high sensitivity and high resolution are very difficult to integrate into one modality. The complementary abilities of different imaging modalities could be harnessed to achieve great positive effects. Imaging modalities used or explored in clinic include magnetic resonance imaging (MRI), computed tomography (CT), PET, SPECT and photoacoustic imaging (PAI). Among the above imaging techniques, MRI and CT generate high resolution anatomical images but the contrast agent sensitivity is very low. SPECT and PET have the advantages of high sensitivity, unlimited penetration depth and quantifiable results. These modalities are widely used for monitoring pharmacokinetics, biodistribution and target site accumulation, but they have limited spatial resolution. PAI is a relative new imaging technique, with high spatial resolution. It provides high contrast, although detection is limited when the technique is used in soft tissues.

Recently various novel integrated NIR-II dual modal imaging approaches have been developed, such as MRI/NIR-II, SPECT/NIR-II, PET/NIR-II and PAI/NRI-II, which exploit the advantages of NIR-II fluorophores. These approaches not only display high sensitivity but also have a deep penetration depth. Although a series of desirable multimodal imaging NIR-II fluorophores have been recently developed, the correlation between NIR-II and other imaging modalities is not clear, and few reports have focused on the critical mechanistic aspects of design. Most applications have specific mechanistic requirements in both fluorophores and devices to achieve the best performance in high definition imaging.

To better understand and optimize both imaging and delivery of therapy to a lesion site, it is crucial to monitor different aspects of the therapeutic process, including pharmacokinetics, biodistribution, target site accumulation, local distribution, kinetics of drug release and therapeutic efficacy. In recent years, NIR-II imaging techniques have been utilized to guide therapy to delineate targeted tissues, monitor the process of therapy (e.g. photothermal therapy, photo controlled chemotherapy and photodynamic therapy) and visualize drug distribution. The visualization of drug delivery and drug release can be very useful in validating and enhancing drug delivery systems, as well as in predicting therapy responses, especially if the functional or molecular imaging information can be quantified.

This tutorial review is not only a comprehensive summary of advancement of NIR-II fluorescence in *in vivo* imaging, but also an investigation thoroughly of multimodal NIR-II imaging probes and theranostics. In this review, we review chemical methods for preparing donor-acceptor (D-A) structures, and the luminescence characteristics, size, morphology and surface characteristics of bright-emission NIR-II fluorophores. The correlation between different imaging modalities in one NIR-II probe and specific applications is highlighted. The use of emerging NIR-II fluorophores applications, in the form of single nanoparticle or hybrid composites, in biomedical imaging or therapy guidance is also reviewed. In addition, the recent advancements of reported NIR-II imaging systems are highlighted.

Lastly, the future perspective and new challenges for the use of NIR-II fluorophores are discussed.

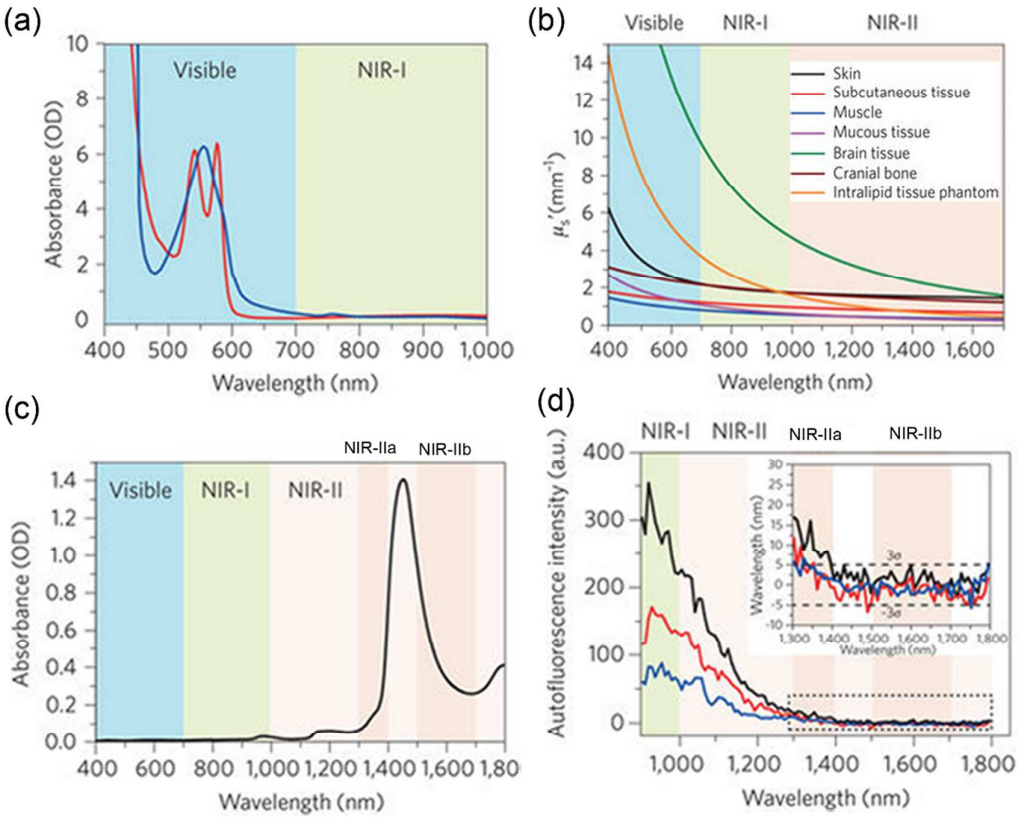

Figure 1. Motivation for NIR-II imaging: (a) Absorption spectra of oxyhaemoglobin (red) and deoxyhaemoglobin (blue) through a 1-mm long path in human blood. (b) Reduced scattering coefficients of different biological tissues and of intralipid scattering tissue phantom as a function of wavelength in the 400-1700 nm region. (c) Absorption spectrum of water through a 1 mm long path. (d) Autofluorescence spectra of *ex vivo* mouse liver (black), spleen (red) and heart tissue (blue) under 808 nm excitation light, showing the absence of autofluorescence in the >1500 nm NIR-IIb window.

(a)-(d): Reprinted (adapted) with permission from ref.[2], Copyright 2017, Nature Publishing Group.

2. NIR-II imaging *vs.* NIR-I imaging

The photons emitted from the NIR-I fluorophores have low energy, and these photons in NIR-I region are not active to react with tissues, leading to a low light scattering and absorbance in the NIR-I window. Compared with the visible imaging in the region of 400-700 nm, the NIR-I imaging in the region 700-900 nm show advantages in deeper tissue penetration depth to visualize anatomical structures, metabolic processes as well as intraoperative NIR-I guided surgical removal of diseased tissues. However, beyond the NIR-I region, the longer wavelength in NIR-II region 1000-1400 nm and 1500-1700 nm will be more favourable windows as the lower scattering coefficients of tissues and autofluorescence, as shown in the declining trends of the scattering curves and slowly decaying of autofluorescence at longer wavelengths (Fig. 1e, f). In the NIR-II region beyond 1500 nm, the autofluorescence almost disappears absolutely. This autofluorescence-free window beyond 1500 nm will further minimize the interference during fluorescence biological imaging.

In recent years, it has been demonstrated that the minimal scattering, low photon absorbance and reduced tissue autofluorescence in the NIR-II fluorophores window can significantly increase signal to noise ratio and penetration depths. For example, in hind limb vasculature imaging, the signal to noise ratio obtained in NIR-II imaging prove to be 4 times (4.8 *vs.* 1.2) higher than that of NIR-I imaging. In addition, we can distinguish the blood vessel at the spatial resolution up to 220 μm in NIR-II window, while it is very difficult to get such high spatial resolution of blood vessel in NIR-I window.[3] In lymphatic vasculature imaging, the small molecule NIR-II fluorophore CH1055-PEG show sharper lymphatic dimension (423 μm) than that blurry lymphatic features acquired from NIR-I fluorophore ICG, owing to both reduced photon scattering and feature size broadening in the NIR-II imaging.[4] In the through-skull non-invasive imaging of brain tumour at up to 4 mm, the NIR-II imaging clearly demonstrates more advantages than NIR-I imaging. Both brain tumours and brain vasculature can be visualized in the NIR-II region in an obvious high degree of clarity, but no any brain tumours and vasculature are observed in NIR-I imaging even using 100 times exposure time than that in NIR-II imaging. In another instance to accurately compare the penetration depth of NIR-II to NIR-I, the intensity of the NIR-I signal at 808 nm rapidly diminishes over increasing tissue depth with complete signal loss by 5 mm. Whereas the NIR-II 1525 nm light can be detected through 10 mm of phantom tissues.[5]

These results suggest that NIR-II imaging provides much higher resolution and more accurate information of deep tissues than NIR-I imaging, inspiring scientist to explore the synthesis of new NIR-II fluorophores and their biomedical applications.

3. Classification of NIR-II fluorophores

The first use of *in vivo* NIR-II fluorescence imaging in mice was reported in 2009.[6] In this pioneering study, low dose single-walled carbon nanotubes (SWCNTs) were used to detect individual vascular tumours noninvasively through the skin monitored by an InGaAs camera, which is operated in the NIR-II spectral range.

Since then, NIR-II fluorescence imaging has become an interesting and fast-growing research area. Developing novel NIR-II fluorophores for *in vivo* imaging applications is very important and expected to have a high impact to many fields in medicine.

Table 1. Comparison of recent developed NIR-II fluorophores: SMDs, SMDCs, SMDNPs, SPNPs, QDs, RENPs and SWCNTs. The corresponding schematic structures are as follows. Acronyms list are: small molecule dyes (SMDs), small molecule dye complexes (SMDCs), small molecule dyes based organic nanoparticles (SMDNPs), semiconducting polymers based nanoparticles (SPNPs), quantum dots (QDs), rare earth doped nanoparticles (RENPs), single-walled carbon nanotubes (SWCNTs), epidermal growth factor receptor (EGFR), Indocyanine green (ICG), gastrin releasing peptide receptor (GRPR), arginylglycylaspartic acid (RGD), Fetal Bovine Serum (FBS), Immunoglobulin G (IgG), Polyethylene glycol (PEG), sentinel lymph nodes (SLN), Human mesenchymal stem cells (hMSCs), Plerixafor (AMD3100), laser vaporization (LV) and deoxyribonucleic acid (DNA).

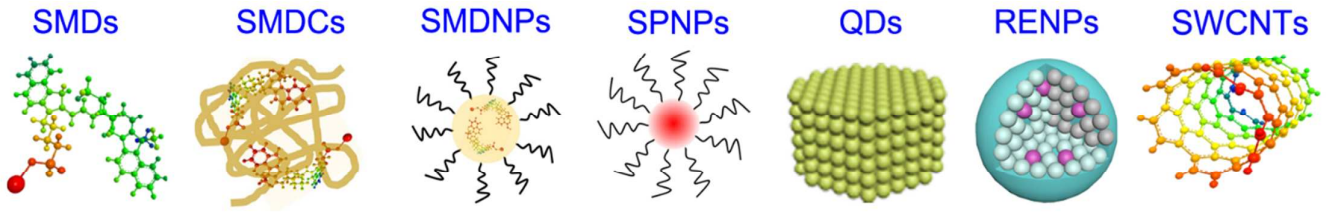

Types	NIR-II fluorophores	Excitation (nm)	Emission (nm)	QYs (%)	Application	Targeting	Refs
SMDs	CH1055	808	900-1350 Peak: 1050	0.3	Imaging of lymphatic vasculatures orthotopic glioblastoma brain tumour and guide surgery	Anti-EGFR affibody	4
	ICG	782	880-1450	0.9	Imaging of vascular and hind limb	Non-specific	7, 8
	CH-4T	808	900-1400 Peak: 1050	0.1	Video rate and ultra-fast imaging of hindlimb vasculature and lymph node.	Non-specific	9
	Q4-1	808	900-1400 Peak:1100	0.2	Multi conjugation sites for NIR-II imaging	Conjugated peptide GRPR targeting	10
	CHS2	808	900-1400 Peak:1050	0.2	Guide surgery and tumour delineation	Conjugated with RGD	11
	IR-E1	808	900-1400 Peak: 1071	0.7	Video rate dynamic brain imaging	Non-specific	12
SMDCs	ICG-FBS	808	880-1200	-	-	-	9
	CH-4T-FBS	808	900-1400 Peak: 1000	5–11	Video rate and ultra-fast imaging of hindlimb vasculature and lymph node.	Strong protein binding affinity	9
	IR-FGP	808	900-1400 Peak: 1050	1.9	3D layer-by-layer molecular imaging	Bioconjugation with streptavidin, Erbitux, EGFR and IgG antibodies	13
	FSH-CH	808	900-1400 Peak:1050	-	NIR-II imaging of testicular tubules, bones, ovarian follicles	Hormonal specificity binding	14
SMDNPs	Q4NPs	808	900-1400 Peak:1100	0.2	Imaging of blood vessels in tumour	Non-specific	10
	SXH and SDH NPs	808	900-1500 Peak:1100	2.0	Imaging of whole body blood vessels and guide SLN surgery.	RGD peptide	15

	CQS1000 NPs	808	900-1300 Peak: 1000	-	Imaging for assessment of angiogenesis of tumour; precise tumour resection, and guide SLN mapping and biopsy	Anti-EGFR affibody	3
	IR1061-PEG NPs	808	900-1300 Peak: 1047	1.8	Entire body imaging,	Non-specific	16
SPNPs	pDA-PEG	808	900-1400 Peak: 1047	1.7	Ultrafast NIR-II imaging of arterial blood flow	EGFR antibody	17
	PDFT1032	808	900-1400 Peak:1032	-	Guide surgery, vascular imaging, SLN biopsy mapping	Non-specific	18
QDs	Ag_2S-6PEG	808	1000-1400 Peak: 1200	15.5	Xenograft 4T1 tumour imaging	Non-specific	19
	Ag_2S-PEG	808	1000-1400 Peak: 1200	16	Lymphatic drainage imaging, blood pool imaging, angiogenesis imaging	Non-specific	20
	Ag_2S-PEG	808	1000-1500 Peak: 1200	15.5	In vivo tracking hMSCs	Tat peptide	21
	$Ag_2S@SiO_2$	785	1000-1200 Peak: 1135	22.7	NIR-II tumour imaging	cRGDfK-R6G peptide	22
RENPs	Y_2O_3: Yb, Er	980	1400-1700 Peak: 1550	-	Organs imaging	Non-specific	23
	$NaYF_4$: Yb: Ln (Ln: Er, Ho, Tm or Pr)	980	1000-1700 Peak:1525, 1185,1475	-	Multispectral tumour imaging	Bioactive albumin	5
	$NaYF_4$: Yb:Er@ $NaYF_4$	980	1310, 1000-1700 Peak: 1525	-	Cancer early detection	AMD3100	24
	$NaYF_4$:Yb^{3+}/X^{3+}@ $NaYbF_4$@$NaYF_4$:Nd^{3+}-ICG, (X = Er, Ho, Tm, or Pr)	808/980	1000-1700 Peak: 1060 1165, 1310, 1460, 1530	13	ICG enhance NIR-II emission	Non-specific	25
SWCNTs	SWCNTs-mPEG	808	1100-1400	0.1	Xenograft 4T1 tumour imaging, video-rate imaging, and 3D reconstruction.	Non-specific	26
	SWCNTs-cholate	808	900-1500	0.4	Intravital tumour vessels imaging	RGD peptide	6
	SWCNTs-DSPE-mPEG	808	1100-1700	0.1	Video rate in vivo imaging	Non-specific	27
	SWCNTs-IRDye800	785/808	1100-1400	-	Video rate of venous vessels imaging; blood perfusion imaging and brain vasculature imaging	Non-specific	28, 29
	Chirality SWCNTs	725	850-1350	-	Vascular imaging	Non-specific	30
	LV SWCNTs	808	1200-1800	0.01	High magnification cerebrovascular imaging	Non-specific	31
	SWCNTs-DNA	780	950-1050	-	Implantable inflammation sensor	Non-specific	32

An NIR-II fluorophore with broad use is expected to have the following properties: low toxicity, bright emission (high quantum yield), low susceptibility to photobleaching (high photostability and chemical stability), and chemically

modifiable to achieve specific targeting to disease lesions. To date, several types of organic and inorganic NIR-II fluorophores have been reported.[3-6, 9, 17, 19] The organic NIR-II fluorophores include small molecule dyes (SMDs), small molecule dye complexes (SMDCs), small molecule dyes based organic nanoparticles (SMDNPs), and semiconducting polymers based nanoparticles (SPNPs). The inorganic NIR-II fluorophores include quantum dots (QDs), rare earth doped nanoparticles (RENPs) and SWCNTs. The photophysical pathways for NIR-II fluorophores in solution and the mechanism of NIR-II fluorescence emission are summarized in Scheme 2. Among these NIR-II fluorophores, SMDs, SMDCs and SMDNPs are scarcely retained within the reticuloendothelial system, showing high promise for future clinical translation. The bandgap of SPNPs is tunable to obtain various emission wavelength in NIR-II window. The size of QDs for NIR-II is small (< 10 nm) and show strong NIR-II emitting because of the high quantum yields up to 10%. RENPs probes act as NIR-II emitting at specific wavelength depending on lanthanide ions in single nanocrystals. SWCNTs have broad emission spectra at wavelengths between 1000 and 1800 nm but with low quantum yields (<0.4%). A comparison of key aspects of the different NIR-II fluorophores is provided in Table 1.

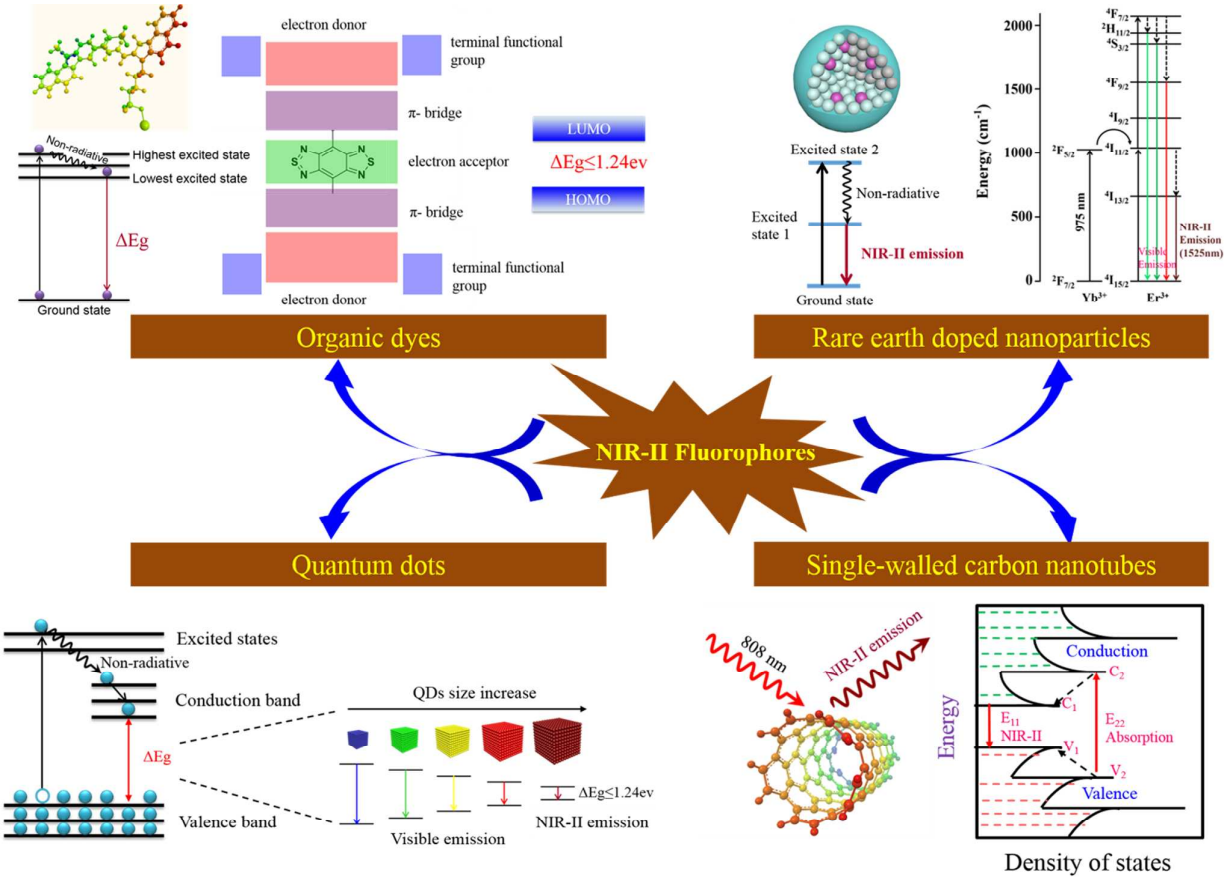

Scheme 2. The photophysical pathways for NIR-II fluorophores in solution and the mechanism of NIR-II fluorescence emission. For organic dyes, with these donor–acceptor–donor compounds, we can shift the emission to longer wavelengths by reducing the energy gap between Lowest Unoccupied Molecular Orbital (LUMO) and Highest Occupied Molecular Orbital (HOMO). For rare earth doped nanoparticles, the NIR-II emission

wavelength depend on the activator dopants, such as Ho, Pr, Tm and Er enable emissions at 1185, 1310, 1475 and 1525 nm, respectively. The emissions of Ho, Pr, Tm and Er doped samples are attributed to the $^5I_6 \rightarrow {}^5I_8$, $^1G_4 \rightarrow {}^3H_5$, $^3H_4 \rightarrow 3F_4$, and $^4I_{13/2} \rightarrow {}^4I_{15/2}$ transitions, respectively. For quantum dots, under the excitation of UV or Visible light excitation, fluorescence emission wavelength is a function of the particle's size with larger particles emitting at longer wavelengths. For the single-walled carbon nanotubes, due to the quantum confinement along the transverse direction of a single carbon nanotube, the NIR-II emission wavelength of single-walled carbon nanotubes in a band gap are mainly dependent on the diameter of the nanotube and the chiral angle.

3.1 Organic NIR-II fluorophores: SMDs, SMDCs and SMDNPs

By now, several types SMDs NIR-II fluorophores with excellent performance are developed and the representative chemical structures are shown in Figure 2. SMDs have different degree of brightness in the NIR-II emission and rapid excretion, and they can be manufactured under Current Good Manufacturing Practice (cGMP) condition. Because of these factors, SMDs are widely recognized as highly attractive and promising NIR-II fluorophores for future clinical applications. The first example using SMDs NIR-II fluorophore for *in vivo* imaging was reported in 2015, named CH1055 (Fig. 3a-d).[4] The fluorophore units are composed of conjugated aromatic units, with a donor-acceptor-donor (D-A-D) structure and a benzobisthiadiazole core. The energy gap could be reduced through π-spacers by attached of strong electron donors. The spatial configuration of strongly electron-donating groups flanking a central electron acceptor shrinks the energy gap separating the hybridized highest occupied molecular orbital (HOMO)/lowest unoccupied molecular orbital (LUMO) levels and shifts the fluorescence emission into the NIR-II window. CH1055 has an emission peak at 1055 nm and with a tail extending emission into the NIR-IIa region (1300–1400 nm). The fluorophore enters the brain vasculature and enables detection of tumours in the brain at depths of 4 mm by a non-invasive through-skull technique. Compared with FDA-approved fluorophore ICG for NIR-I imaging, CH1055 based NIR-II imaging provides higher resolution in diagnosis sentinel lymph nodes (SLN) for surgical resection. Pharmacokinetic studies of ICG-PEG demonstrate rapid urinary excretion, comparable to that of ICG, with 90% excretion via the kidneys in 24 h. Tumour-specific targeting NIR-II fluorescent probe can also be obtained by conjugating CH1055 with an anti-epidermal growth factor receptor (EGFR) affibody molecule. The affibody-conjugated CH1055 specifically targets xenograft human squamous cell carcinoma tumours in immune-deficient mice and allows accurate image-guided tumour-removal surgery. NIR-II window molecular imaging gives a 5-fold higher tumour-to-normal tissue ratio than that in the NIR-I window. In another work, Feng et al. conjugate CH1055 to follicle stimulating hormone (FSH) and used the resulted NIR-II probe to specifically image ovaries in live mice. They are also able, for the first time, to detect specific FSH receptor in bones. According to the expression of FSH receptors, it could resolve earlier controversies in cultured osteoclasts.[14] Furthermore, investigation of the structure-absorption/fluorescence properties of a small library of fluorescent compounds in which the core structure of CH1055 had been modified allows the identification of another small molecule NIR-II fluorophore Q4 due to the attractive properties. Conjugation of Q4 with a

GPCR-targeting peptide, RM26, provides a new targeted NIR-II probe, SCH1100, which is successfully used for the specific imaging of prostate cancer *in vivo*.[10]

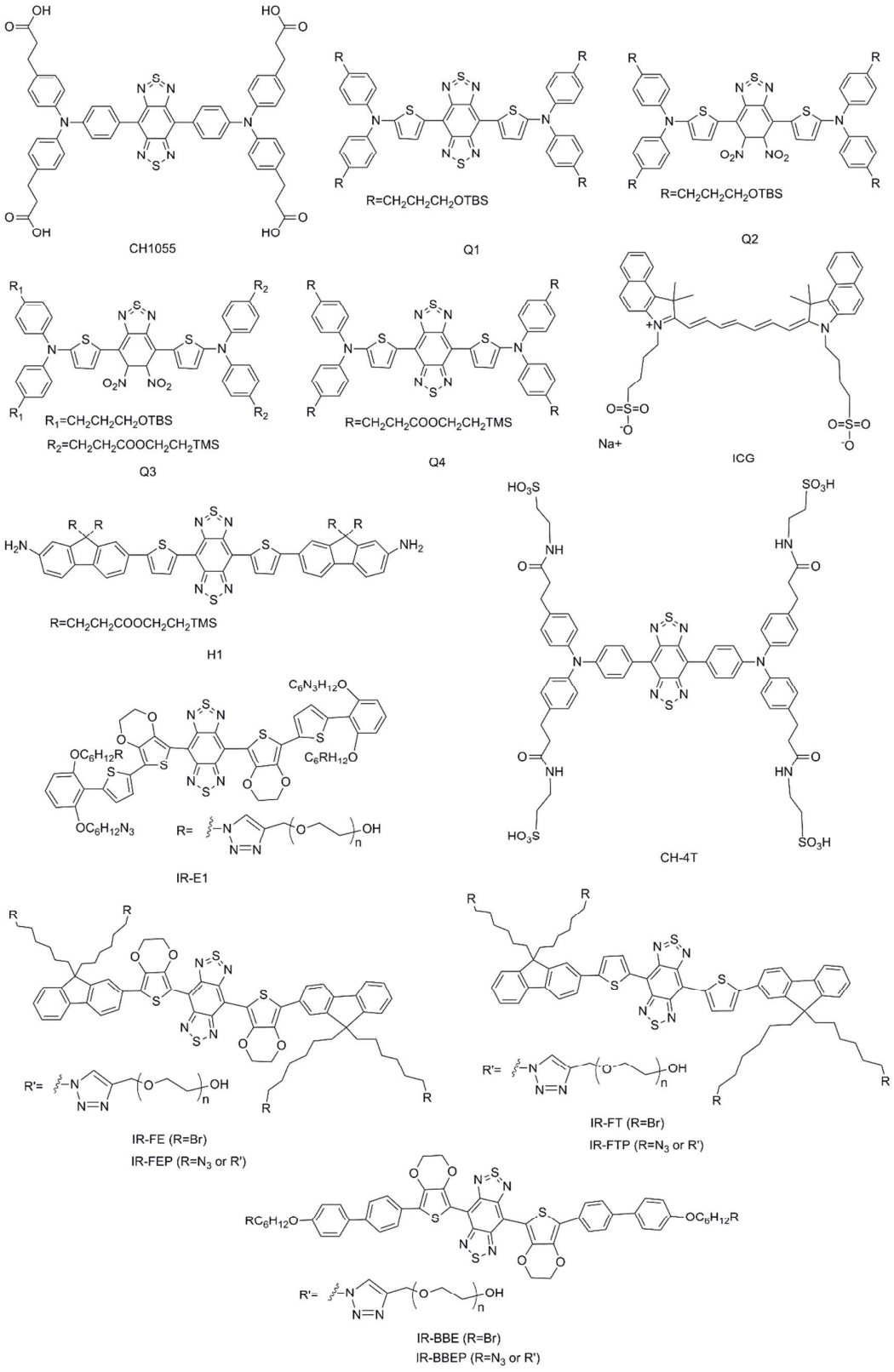

Figure 2. Current representative small molecular NIR-II fluorophores

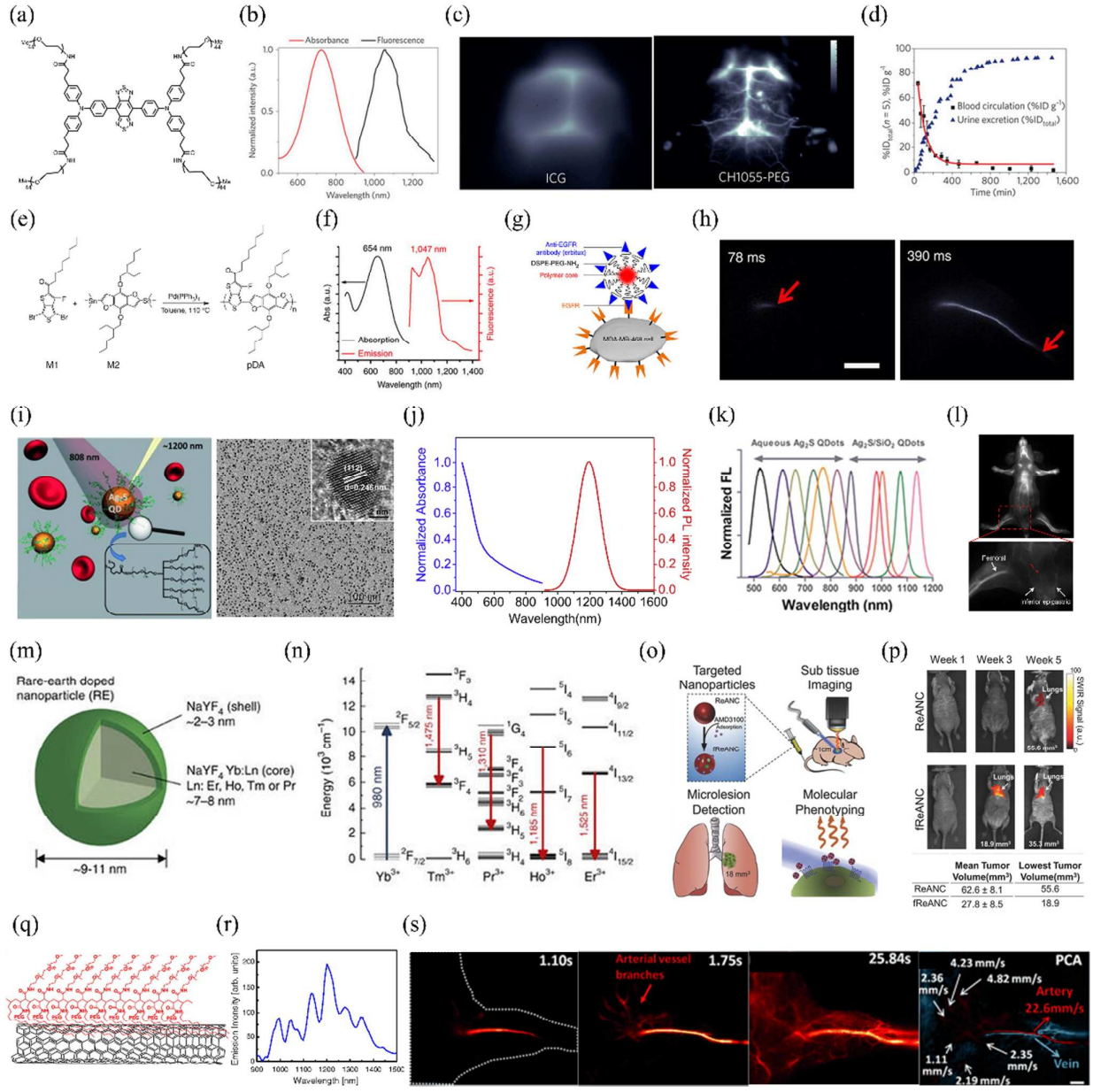

Figure 3. Advancement of NIR-II fluorophores and imaging in vivo. (a) Chemical structure of CH1055. (b) Absorbance and fluorescent emission of CH1055-PEG (808 nm excitation). (c) Brain vasculature imaging through the scalp and skull in mice using either ICG or CH1055-PEG. (d) PEGylated CH1055 (8.9 kDa) shows 90% renal clearance in the first 24 h post-injection. (e) Scheme for the Synthesis of pDA SPNPs NIR-II polymer. (f) Absorption and emission spectra of pDA-PEG. (g) A schematic showing the structure of pDA-PEG-Erbitux bioconjugate. (h) Ultrafast NIR-II imaging of arterial blood flow. (i) Scheme of 6PEG-Ag_2S QDs that emit at 1200 nm upon excitation at 808 nm and the TEM image of the Ag_2S QDs. (j) Absorbance and photoluminescence spectra of PEGylated Ag_2S QDs. (k) The tunable of NIR-II emission of Ag2S QDs. (l) Intravital NIR-II fluorescence image of the nude mouse in supine position. The PL signal from the Ag_2S QDs is easily distinguishable from the endogenous autofluorescence without any image processing. (m) Rare earth nanoprobes

consist of a $NaYF_4$: Yb:Ln-doped core (Ln: Er, Ho, Tm or Pr) surrounded by an undoped shell of $NaYF_4$. (n) Probes consisting of a $NaYF_4$ host doped with Yb, Ho, Pr, Tm and Er enable emissions at 1185, 1310, 1475 and 1525 nm, respectively. The emissions of Ho, Pr, Tm and Er doped samples are attributed to the $^5I_6 \rightarrow {}^5I_8$, $^1G_4 \rightarrow {}^3H_5$, $^3H_4 \rightarrow {}^3F_4$, and $^4I_{13/2} \rightarrow {}^4I_{15/2}$ transitions, respectively. (o) AMD3100 was adsorbed onto the surface of fully formed ReANCs to generate AMD3100 functionalized ReANCs or fReANCs. Athymic nude mice were inoculated with human breast cancer cells through the tail vein. Animals were treated with either ReANCs or fReANCs and NIR-IIB imaging performed to determine nanoprobe-tumour localization. (p) Longitudinal tracking of internal lesions with NIR-IIB imaging. Mean and minimum volume of tumours detectable via NIR-IIB imaging was calculated to determine the smallest tumours capable of resolution using the InGaAs camera. (q) Schematic of the water-soluble SWCNTs conjugated with C_{18}-PMH-mPEG (90 kDa). (r) Fluorescence spectrum of SWCNTs excited at 808 nm, showing several emission peaks spanning the NIR II region. (s) Video rate NIR-IIb fluorescence imaging of mouse hindlimb vessels (n=3) and dynamic contrast-based vessel type differentiation. PCA overlaid image showing the differentiation of arterial (red) and venous (blue) vessels, Scale bar: 2 μm.

(a)-(d): Reprinted (adapted) with permission from ref.[4], Copyright 2015, Nature Publishing Group.

(e)-(h): Reprinted (adapted) with permission from ref.[17], Copyright 2014, Nature Publishing Group.

(i): Reprinted (adapted) with permission from ref.[19], Copyright 2012, Wiley-VCH Verlag GmbH & Co. KGaA.

(j) and (l): Reprinted (adapted) with permission from ref.[20], Copyright 2014, Elsevier B.V.

(k): Reprinted (adapted) with permission from ref.[22] Copyright 2012, American Chemical Society.

(m)-(n): Reprinted (adapted) with permission from ref.[5], Copyright 2013, Nature Publishing Group.

(o) and (p): Reprinted (adapted) with permission from ref.[24], Copyright 2015, Wiley-VCH Verlag GmbH & Co. KGaA.

(q): Reprinted (adapted) with permission from ref.[26], Copyright 2012, American Chemical Society.

(r): Reprinted (adapted) with permission from ref.[27], Copyright 2011, National Academy of Sciences.

(s): Reprinted (adapted) with permission from ref.[31], Copyright 2015, Wiley-VCH Verlag GmbH & Co. KGaA.

Another interesting small molecular dye, named IR-E1 was reported recently (Figure 2). This novel NIR-II fluorophore exhibits higher quantum yield (0.7%) than CH1055 (QY=0.3%) as well as fast renal excretion (83%) within 24 h post injection. In addition, it achieves high resolution dynamic imaging of the vascular changes particular in a traumatic brain injury model, including initial transient hypoperfusion due to NIR-II fluorophore leakage and accumulation caused by cerebrovasculature damage.[12]

Interestingly, in 2017, small molecule dyes ICG and IR800, for the first time were reported with the enhanced the NIR-II fluorescent brightness (tail up to 1150 nm) via assemblies with FBS (Ref. 9 in the SI Fig. S14).[9] Followed this research work, by switching the detection from conventional silicon-based NIR cameras to emerging, high performance InGaAs SWIR cameras, Bruns et al find that ICG exhibit higher quantum yields (0.9%) in aqueous solution than IR-E1050 (quantum yields 0.2%) in the NIR-II emission region (detectable up to 1575 nm).[8] Moreover, Starosolski et al demonstrate that ICG display a significant enhanced NIR-II (1000–1250 nm) emission in plasma and low polar solvents such as ethanol.[7] *In vivo* imaging results have demonstrated that the signal noise ratio values of use of ICG in the NIR-II window is two times than that of in the NIR-I window.[7] These findings open a quick route for translation of NIR-II imaging technique into clinical applications. Generally,

the following categories of dye-solvent and dye-dye interactions in non-polar or polar solvents may play a vital role in deactivating excited state fluorophores. Several important factors are (i) electrostatic interactions, (ii) weak associations with defined stoichiometry and structure, (iii) hydrogen bonding between dye-solvent and dye-dye. Besides, for such low energy gap NIR-II fluorophores, a large variety of complicated and uncertain processes are involved in the deactivating excited state. The following categories may play a vital role for deactivating excited states: (i) the intermolecular interactions between NIR-II fluorophores; (ii) strong complex formation in the excited state and strong complex formation in the ground state. Excitation can cause structural reorganization and deactivating excited states process may be fast; (iii) dye diffusion in solvent processes may deactivate excited states; (iv) dielectric of NIR-II fluorophores may affect the proton translocation and electron transfer leading to deactivating excited states.

However, most of the SMDs are hydrophobic and need to be encapsulated into surfactant (e.g. PEG, liposome) or conjugated with protein to formed NIR-II SMD complexes or SMD nanoparticles, named as SMDCs and SMDNPs, respectively. Although CH1055 has excellent pharmacokinetic properties, factors such as low quantum yield (0.3%), fluorophore absorbance, emission wavelength and synthetic complexity could be improved. Low quantum yield NIR-II fluorophores limit penetration depths and cause low temporal resolution. Diversified fluorophore absorbance and emission in NIR-II would offer more options. By replacing the carboxylic acid groups of CH1055 with more negatively charged sulfonic acid groups and using supramolecular assemblies with serum proteins, Antaris et al. produce a water soluble SMDCs NIR-II dye in FBS (CH-4T-FBS) and show a 110-fold fluorescence enhancement.[9] CH-4T-FBS allows fast video-rate imaging at a 50 frames-per-second in the NIR-II window and reduces exposure time more than 50-fold compared to ICG. CH-4T-FBS clearly demonstrates the benefits of the NIR-II window for imaging deep anatomical features.

Novel SMDNPs NIR-II fluorophores, SXH and SDH are prepared and used for integrin $\alpha_V\beta_3$-targeted glioma imaging recently.[15] These NIR-II organic nanoparticles enable to delineate tumours from surrounding normal tissue and can be further applied for image guided surgery. It is worth noting that SXH and SDH NIR-II probes are based on a small molecular H1. In H1 chemical structure, 2-Amino 9,9-dialkyl-substituted fluorene moieties are induced into the CH1055 structure. They can distort the benzobisthiadiazole core and tune the distribution of electrostatic potential and the bandgap to a desired range effectively. The fluorene moieties not only act as electron donors, but also as protecting groups that shield the backbone from aggregation. In another work, a multifunctional NIR-II probe, CQS1000 SMDNPs, are prepared by encapsulating CH1055 into phospholipid vesicles.[3] CQS1000 can be used to noninvasively and dynamically visualize and monitor many physiological and pathological conditions of circulatory systems. Processes that can be monitored include drainage and routing lymphatic, tumour angiogenesis and vascular diseases. Compared with traditional NIR-I imaging, CQS1000 offers the promise of improved guidance for surgery by sentinel lymph node mapping. This new

NIR-II fluorophore allowed complete and precise resection of tumours by distinguishing the blood supply and lymphatic drainage, which may lead to better survival and reduced relapse rates. Another novel water soluble NIR-II SMDCs IR-FGP was synthesized using click chemistry recently reported by Zhu et al.[13] IR-FGP not only demonstrates a bright NIR-II emission by tuning a D-A-D architecture systematically, but also offers many targeting channels. In addition, this IR-FGP NIR-II SMDCs nanoprobe allows 2D and 3D tomographic imaging in deep tissue and reduces the autofluorescence, which strongly benefits a broader spectral imaging window in NIR-II.

It is worthy to note that SMDs, SMDCs and SMDNPs NIR-II fluorophores still need further improvement. The versatility of SMD, SMDCs and SMDNPs NIR-II fluorophores for precise visualization and evaluation of biological processes also needs to be investigated thoroughly. Importantly, many unmet clinical needs could be evaluated and potentially addressed by the use SMD, SMDCs and SMDNPs NIR-II fluorophores.

3.2 Organic NIR-II fluorophores: SPNPs

SPNPs are semiconducting organic macromolecules that are characterized by a backbone chain of alternating double- and single-bonds. They have been widely used in organic solar cells, diodes and electronics. Fluorescence imaging of SPNPs has been limited to emission wavelengths < 900 nm. Shifting their emission, specifically into the NIR-II window, is challenging but essential to broad their biomedical applications. Increasing π-conjugation length by designing quinoid-stabilized D-A polymers is an effective strategy for reducing bandgap and bringing about a bathochromic shift into the NIR-II window. Hong et al. have described a facile synthetic method for SPNPs in NIR-II region with tunable bandgap energy by D-A alternating copolymerization. One of these copolymers, poly (benzo [1,2-b:3,4-b'] difuran-alt-fluorothieno-[3,4-b'] thiophene) (pDA), show NIR-II emission peak at 1050 nm and a high quantum yield up to 1.7%, which is much brighter than that of typical SWCNTs (~0.4%) used previously (Fig. 3e-h).[17] Because of the unique charge-transfer structure between donor and acceptor, the pDA NIR-II fluorophore shows red-shifted absorption and emission compared to the corresponding homopolymers. This leads to a series of SPNPs with tunable excitation and emission wavelengths for NIR-II imaging. Conjugation of PEGylated pDA with Cetuximab (Erbitux), an antibody against EGFR, using standard crosslinking reactions between $-NH_2$ groups and -SH groups, gave pDA-PEG-Erbitux. When used for NIR-II fluorescence imaging, the antibody-conjugated probe selectively targets EGFR-positive cells over EGFR-negative cells. This NIR-II fluorophore allows imaging of dynamic changes in blood flow at a frame rate of over 25 frames-per-second, pushing the temporal resolution limitation to a previously unattainable level. In addition, this pDA SPNP NIR-II fluorophore can track blood flow in capillaries with diameters as lower as 10 mm, which is even below the spatial resolutions using ultrasound and optical coherence tomography (OCT). The combination of the pDA NIR-II fluorophore and detector sensitivity gives a dynamic

range of blood velocity from 0 to 640 mm/s. The pDA-PEG NIR-II fluorophore can also track regional blood flow and redistribution thus provides diagnostic tool for visualizing metabolic differences in tissues directly. This study opens the possibility of NIR-II fluorescence probes that can achieve haemodynamic imaging with high spatial and high temporal resolution by minimizing scattering with high quantum yields and ultrashort imaging exposure time. However, one limitation of pDA SPNP should be considered is that photodegradation upon 808 nm excitation for 1 h results in NIR-II fluorescence intensity decline up to 20%. Another major drawback of pDA SPNP is the potential risk of high toxicity.

Very recently, a high photo-stability SPDP, PDFT1032 is developed.[18] PDFT1032 is synthesized based on a strong planar electron acceptor - diketopyrrolopyrrole (DPP), which is able to couple with many electron donors easily and tune the bandgap to obtain expected fluorescence emission. PDFT1032 not only exhibits excellent maximum absorption wavelength at 809 nm, but a large stokes shift of 223 nm to 1032 nm under 808nm excitation. In addition, PDFT1032 demonstrate excellent performance in real time imaging including tumour diagnosis and SLN mapping. Moreover, in NIR-II image guided tumour surgery and embolization therapy, PDFT1032 displays high spatial resolution (μm range) and high temporal resolution (>25 frames per second). These excellent properties highlight PDFT1032 NIR-II SPNP as a promising and widely applicable NIR-II probe in pre-clinical and potentially clinical imaging.

3.3 Inorganic NIR-II fluorophores: QDs

Amongst the seven classes of NIR-II emitting probes reported until now, QDs show the highest fluorescence quantum yields (up to 15.5%).[19] The current most desirable brightly fluorescent NIR-II QDs, such as PbS and Ag_2S, act as versatile NIR-II QDs fluorophores because of high resistance to photobleaching, tunable band gaps and large multiphoton absorption cross-sections.

The first and most promising NIR-II fluorescent QDs to be used in the pre-clinic research is Ag_2S, which does not incorporate a toxic heavy metal and show high uptake in tumours (Fig. 3i).[19] Ag_2S QDs have been used in imaging of blood vasculature with micrometre level resolution (up to 40 μm) of the peripheral vasculature and tumour angiogenesis during cancer growth and metastasis. It is critical to monitor new blood vessels formation, both around and within tumours, for surgical treatment, assessment of blood supply in tissues and screening of anti-angiogenic drugs. Ag_2S QDs based NIR-II imaging shows excellent clarity and penetration depth for visualizing lymphatic vessels and lymph nodes during sentinel lymph node resection than the FDA-approved, clinical standard contrast agent, ICG based NIR-I imaging (Fig 3j and l).[20] In addition, Ag_2S QDs is able to track and visualize mesenchymal stem cells (MSCs) populations during intricate biological processes.[21] It provides a promising method to monitor the MSCs transplantation and acquires the important information about cell dynamics and interactions with the host central nervous system. Furthermore, Ag_2S QDs offer a chance for enhancing both early disease diagnosis sensitivity and identification of lesions by targeting functional

molecules (e.g. proteins, peptides, folic acid and antibodies). For example, conjugation of 9 nm Ag_2S QDs with a cyclic pentapeptide that binds to the $\alpha_V\beta_3$ integrin receptor, which is upregulated on the surface of tumour cells, the uptake efficiency has been improved 8–10-fold. Imaging sensitivity is significantly enhanced by creating brightly targeting NIR-II emitting fluorophore to specific sites (Fig. 3k).[22]

Despite different strategies have been explored for using QDs for high quality NIR-II bioimaging, several points should be noted. Firstly, leakage of encapsulated NIR-II QDs from the surfactants in a physiological micro-environment causes toxicity *in vivo*. Secondly, protein or polymer coatings increase the particle size and the pharmacokinetics may be changed. Thirdly, quenching of NIR-II emission can be facilitated by functional groups (e.g. hydroxyl groups and hydrocarbons) attached onto the QDs surface. Fourthly, the functionalization process may cause elements leaching or etching, which leads to an NIR-II wavelength shift (i.e. blue shift).

3.4 Inorganic NIR-II fluorophores: RENPs

RENPs composed of lanthanides ions (from La to Lu, together with Sc and Y) embedded within an inorganic crystalline host matrix (e.g. $NaYF_4$, GdO_2S_2 and CaF_2) have attracted considerable attentions in the field of material science and optical imaging. Because of their large Stokes shifts, narrow and multi-peak emission profiles, long lifetime and excellent photostability, RENPs have been considered as promising alternatives to conventional organic fluorophores and QDs for NIR-II imaging. The NIR-II fluorescence of RENPs occurs because of resonant energy transfer from sensitizer to an RE-activator dopant, such as erbium (Er), thulium (Tm), holmium (Ho), neodymium (Nd) or praseodymium (Pr), whose relaxation generates unique activator-dependent downshifting. Yb/Er co-doped ceramic phosphors with emitting peak at 1550 nm have been modified with PEG-b-poly(4-vinylbenzylphosphonate) (PEG-b-PVBP) and PEG possessing a mono-phosphonate end group ($PEG\text{-}PO_3H_2$) and the resulting RENPs have been successfully used for organs NIR-II imaging in mice.[23]

Highly monodisperse RENPs are typically formed in high boiling organic solvents via thermal decomposition. The poor aqueous solubility of surfactant on the surface of the nanoparticles prevents subsequent functionalization for biomedical applications. Surface modification is thus crucial for improving the dispersion of RENPs in water. For example, by encapsulating RENPs with FDA-approved albumin, Naczynski et al. successfully demonstrate real time, multispectral *in vivo* NIR-II imaging, which offers anatomical resolution using a library of tunable RENPs (Fig. 3m-n).[5] This work introduces a new generation of versatile NIR-II nanoprobes that facilitate disease monitoring using minimally invasive NIR-II imaging. Interestingly RENPs have also been excited by X-ray instead of laser to produce emission light for NIR-II imaging, highlighting their potential use to obtain both anatomic and molecular information through CT and NIR-II imaging.[33] Improvements in sensitivity to enable detection of much smaller cancerous lesions can be made by further surface functionalization of RENPs with specific targeting moieties. For example, targeting NIR-II fluorophores have been prepared by encapsulating RENPs with AMD3100, a

hydrophobic small molecule antagonist of the chemokine receptor CXCR4. These targeting RENPs preferentially localize to receptor-positive tumours in mice, allowing detection of CXCR4-positive tumours 4 times smaller than receptor-negative tumours (Fig. 3o-p).[24] These targeted NIR-II fluorophores enable imaging of microlesions in the lungs at a depth of ~1 cm and are able to simultaneously identify the phenotype of the tumour population. This study is significant to functionalize NIR-II RENPs to detect sub-tissue microlesions at an early stage.

The optical efficiency of these RENPs is, however, quite low (< 0.5%), and there is ample scope for this to be improved to maximize the full potential benefits of RENPs based bioimaging. For example, hybrid organic-inorganic nanocrystals incorporating the contrast agent ICG demonstrate a large Stokes-shift (> 200 nm) with multiple narrow band emissions in the NIR-II range. The ICG not only enhances the NIR-II brightness by ~4-fold but also produces a broad excitation band at 700–860 nm. The ICG-sensitized nanocrystals allow clear observation of a sharp NIR-II image through chicken breast tissue, with signal detection at a depth of 23 mm.[25]

3.5 Inorganic NIR-II fluorophores: SWCNTs

SWCNTs have unique intrinsic physical and chemical properties (e.g. Raman scattering cross-sections, UV/visible/NIR absorption). The biological and biomedical applications have been widely explored over the past two decades. Because of van Hove transitions across bandgaps, semiconducting SWCNTs demonstrate intrinsic fluorescence in the NIR-II window (Fig. 3q-r).[26] Generally, SWCNTs are hydrophobic and require surface functionalization with water soluble polymers or proteins that allow them non-toxic.[6, 27] In 2009, NIR-II probes were prepared for the first time by coating SWCNTs with phospholipid-polyethylene glycol, using an exchange procedure with sodium cholate. This indicates the beginning of the use of SWCNTs for NIR-II imaging.[6] Since then, SWCNTs have been extensively used for dynamic contrast-enhanced NIR-II imaging through principal component analysis (PCA). Applications include tumour-specific imaging,[26] mouse organ registration,[27] and haemodynamic imaging of mouse peripheral vessels, with higher spatial resolution than that afforded by *in vivo* microCT.[28, 30]

Non-invasive brain imaging is still largely reliant on CT and MRI but these techniques are being challenged by fluorescence imaging. For the first time, SWCNTs have allowed for NIR-II imaging of mouse cerebral vasculature, with high spatial (< 10 μm) and temporal (< 200 ms per frame) resolution, at a depth of > 2 mm in an epifluorescence imaging mode.[29] This is a truly non-invasive procedure that does not require invasive surgical procedures. The study leads to high spatial and temporal resolution, real-time dynamic cerebrovascular imaging at molecular level. Although longer fluorescence emission would further reduce scattering, the region between 1400 and 1500 nm is typically avoided because of the presence of a water overtone absorbance peak.[1, 31] The long wavelength NIR-II region (1500–1700 nm) provides a balance between photon scattering and water-absorption effects, and it is able to achieve deeper penetration depth and resolution. For example, SWCNTs with smaller band gaps and larger average diameters (up to 1.24 nm) were recently synthesized by

laser vaporization. They allow *in vivo* vascular NIR-II imaging at a depth of up to 3 mm in mouse hindlimb and brain with intact skull and scalp, with high spatial resolution (~4 mm). Single-vessel-resolved blood flow speed mapping for multiple hindlimb arterial vessels has also been obtained simultaneously by video-rate fluorescence NIR-II imaging (Fig. 3s).[31]

Early detection of cancer ultimately improves patient survival. Detection sensitivity can be improved by creating targeted bright-emission SWCNTs as NIR-II emitting probes. For example, a genetically engineered multifunctional M13 phage has been assembled with SWCNTs via π–π interactions for use as a ligand for targeted NIR-II imaging of tumours. Compared with control non-targeted SWCNTs, targeting M13-SWCNTs improves the uptake up to 4-fold in prostate-specific membrane antigen-positive prostate tumours. Detection and excision of deep, small metastatic tumour nodules by a gynaecological surgeon is also improved with M13-SWCNTs leading to the identification of sub-mm tumours that are not easily identified by either visible or NIR-I fluorophore.[34] Other suitable targeting strategies, such as analyte-specific receptors, which can transform SWCNTs into an NIR-II biosensor for detecting trace of biomolecules, have also been developed recently. For example, A-DNA-wrapped SWCNTs show selective changes in NIR-II signal output in response to different NO concentrations and are capable of detecting changes in NO level in response to wound-induced tissue inflammation.[32] Careful engineering of SWCNTs surfaces to achieve high chemical stability and resistance to photobleaching will enable SWCNTs to have many promising applications. It should be noted, however, that SWCNTs display high infrared absorbance, which may cause NIR-II loss. Local temperature increases could also result in thermal injury. Achieving lower power excitation and higher quantum yields will thus be a major focus in future SWCNTs research.

4. NIR-II fluorophores based multimodal imaging

NIR-II is a rising imaging technique offering high spatial-temporal images of deep tissue, along with inherent advantages of real time imaging capability and high sensitivity. It can be used to visualize many dynamic processes in real time, such as cancer development and metastasis, cell trafficking, cellular events in immune reactions, etc. Despite this, there are still many limitations that need to be addressed because of the nature of optical imaging techniques. First, tissue penetration by NIR-II is still limited compared with many other modalities such as MRI, CT, PET, SPECT, and US, which can be used for whole body imaging. Second, it is still very difficult to evaluate NIR-II images quantitatively in vivo. Third, NIR-II imaging can provide molecular and physiological but not anatomic information of diseases. Therefore, it is highly desired to develop NIR-II based multimodal imaging techniques to overcome the limitations of NIR-II alone.

(1) Single component based multimodality imaging

In designing of multimodality imaging probe, sometimes a single component in the probe can be used to generate signals for different imaging modalities. For example, many fluorescent dyes can be used for both PAI and NIR imaging. PAI is an

emerging optical imaging modality in which absorbed photon energy is converted into acoustic waves that are detected using ultrasound. PAI provides higher spatial resolution and better contrast than conventional optical imaging techniques, because ultrasound scattering in tissues is ~2–3 orders of magnitude lower than optical scattering. PAI also has high sensitivity and allows quantitative 3D visualization, making it particularly suitable for diagnosis and assessment of a variety of diseases including tumour. Recently, donor-acceptor chromophore based nanoparticle (DAP) has been synthesized by nanoprecipitation process to encapsulate the NIR-II chromophore CH1000 molecules within amphiphilic phospholipids. Moreover, to enhance tumour targeting efficiency, the EGFR affibody is conjugated with DAP successfully. This affibody-DAP organic nanoprobe demonstrates capability to selectively target EGFR-positive tumours in an FTC-133 subcutaneous mouse model with enormous enhanced both PAI and NIR-II fluorescence contrast in both *in vitro* and *in vivo* (Fig. 4a).[35]

RENPs have been established as NIR-II fluorescent probes with sharp absorption and emission peaks. In addition, they can be precisely tuned principles in any NIR-II emission by changing the RE dopants. Part of the absorbed light could be converted into radiative fluorescence emission, whilst others are converted into non-radiative energy forms that can be used for PAI. Consequently, the lost non-radiative energy that was previously considered to be a disadvantage in fluorescent probes can now be harnessed to contribute to PA signal enhancement. Typically, fluorescence and PA are complementary signal forms. Materials exhibiting bright fluorescence emission would have weak PA signals, whilst weak fluorescence emission would be accompanied by strong PA signals. A recent study indicates that both the NIR-II fluorescence emission and the PA signal amplitude can be increased by controlling the size and manipulating the thickness of the inorganic shell coating.[36] Size-dependent Ag_2S nanodots (Ag_2S-NDs) for PAI/NIR-II imaging and simultaneous photothermal therapy have been recently synthesized by precisely controlled growth of Ag_2S in albumin nanocages.[37] Ag_2S-NDs produce size-dependent NIR-II fluorescence and good photothermal conversion in the blood circulation. The Ag_2S-NDs show high resistance to photobleaching, good cellular uptake, preferable accumulation in tumours and *in vivo* elimination. All of advantages enable Ag_2S-NDs to be utilized in ultrasensitive fluorescence imaging in NIR-II region, PAI with microscopic spatial resolution and photothermal ablation of tumours.

(2) Two components based multimodality imaging

The typical design of multimodality imaging probe involves the assembling multiple reporters together and integrating them into one entity. Recently, Li et al. have reported a Gd-Ag_2S nanoprobe that combines deep tissue penetration capability of MRI with high spatial-temporal resolution of NIR-II fluorescence imaging (Fig. 4b-d).[38] The localization of the brain tumour can be clearly delineated pre-operatively using MRI signal generated from Gd component in the nanoprobe, and then precise resection of the tumour can be guided by intraoperative NIR-II fluorescence imaging produced by Ag_2S. Integration of MRI and NIR-II fluorescence imaging techniques for tumour detection and resection provide opportunities for future clinical

applications. Compared with Gd, iron oxide nanoparticles (IONPs) have much higher relaxivities and are often used for T_2-weighted imaging. A MRI/NIR-II imaging probe, comprising IONPs and DNA-encapsulated SWCNTs complexes, is successfully prepared to show NIR-II emission and a high magnetic relaxation time scale ratio ($T_1/T_2 = 12$) and a long spin-spin relaxation time (T_2 ~164 ms), which is better than that of the typical ferromagnetic nanoparticles.[39] A novel PET/NIR-II dual modal imaging platform ^{68}Ga-SCH2 is developed using base-catalyzed highly efficient and selective assembly method recently.[11] This small molecule based PET/NIR-II probe can be successfully used for $\alpha_V\beta_3$-targeted tumor imaging. The excellent NIR-II and PET dual modal imaging properties such as high signal to background ratio and specificity lead to tumour-free resection in the small animal models. These inspiring results show high potential for tumor surgery and translational clinical.

A new PAI/NIR-II nanoprobe, ICG@PEG-Ag_2S, has recently been fabricated by simple self-assembly of dot-based theranostic Ag_2S (DT-Ag_2S) QDs, amphipathic C18-PEG and ICG.[40] This novel PAI/NIR-II nanoprobe is retained in the blood for up to 6.88 h. The probe selectively accumulated in the region of atherosclerotic plaques because of the attraction of the lipophilic C18 chain to the atherosclerosis microenvironment and provided a contrast-enhanced PA signal. The use of Ag_2S QDs allowed high spatial resolution fluorescence imaging in the NIR-II window in real-time. Combination high NIR absorption dyes with NIR-II imaging should allow the development of novel strategies for the design of multimodal probes for imaging, targeting and treatment of disease in the clinic.

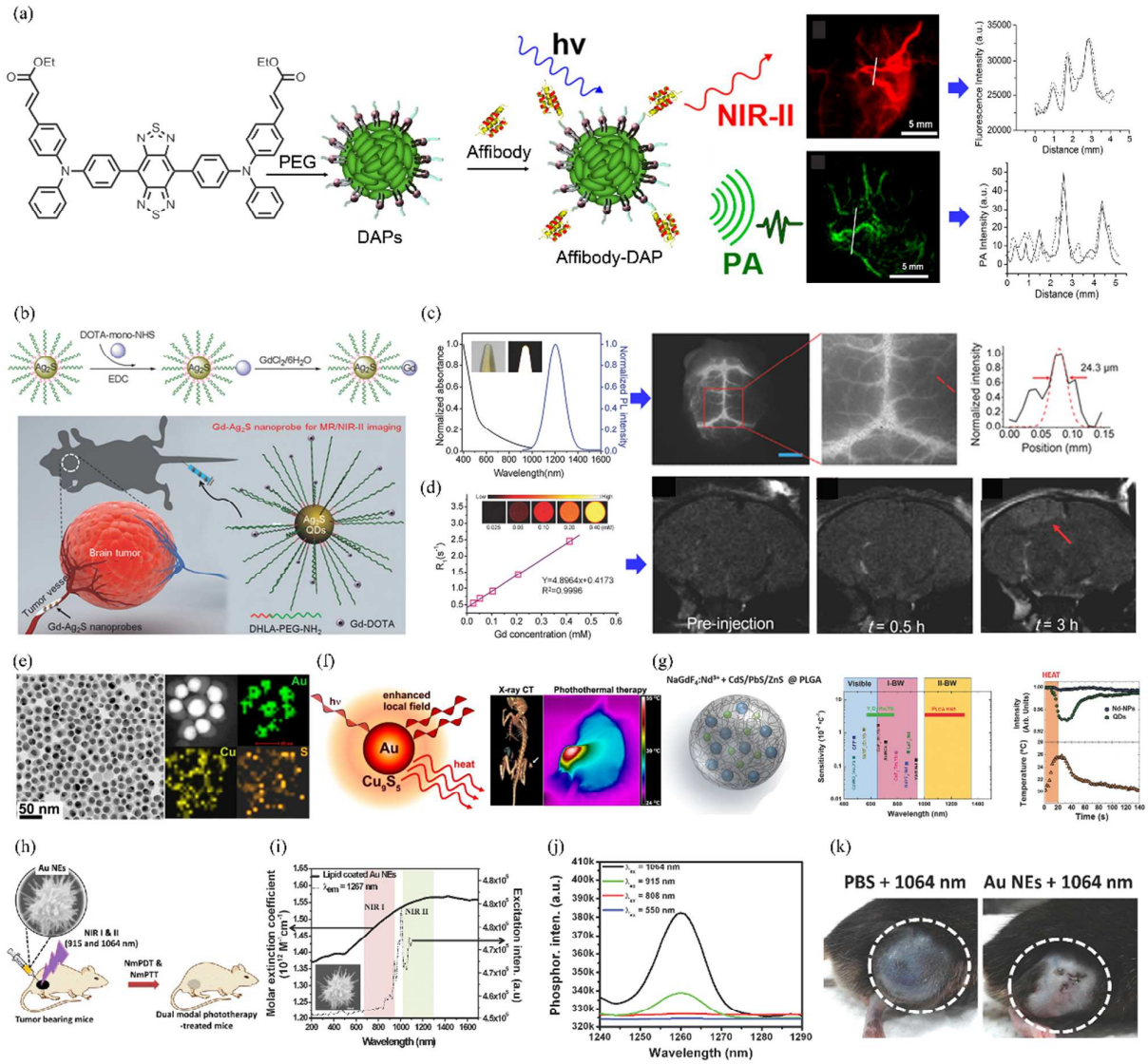

Figure 4. Progress of NIR-II fluorophores based dual-modal imaging and phototherapy *in vivo*. (a) Schematic illustration of preparation of Affibody-DAPs and the dual modal PA imaging and NIR-II imaging. Fluorescence image of the FTC-133 thyroid tumour in the NIR-II and the cross-sectional fluorescence intensity profiles along a white line across FTC-133 tumour. 3D volume rendering of photoacoustic images of the thyroid tumour in a mouse before and after the injection of DAPs. Scale bar = 5 mm. The cross-sectional PA intensity profiles along a white line across FTC-133 tumour. (b) Schematic illustration of the procedure for preparing Gd-Ag_2S nanoprobe and the diagram of brain tumour targeting of Gd-Ag_2S nanoprobe. (c) Absorption and emission spectra of Gd-Ag_2S nanoprobe. (d) Intravital NIR-II fluorescence image of the brain vessels in the nude mouse (left). Amplified fluorescent image of vasculature in the nude mouse (middle). A cross-sectional intensity profile measured along the red-dashed line in (middle) with its peak fitted to Gaussian functions (right). Scale bar represents 3 mm. Relaxation rate R1, the inset shows a T1 map of a MR imaging phantom containing Gd-Ag_2S nanoprobe with different concentrations. In vivo progressive T1-weighted MR images of the U87MG brain tumour at different time points from transverse view and immunohistochemical staining of vessels in brain tissues and tumour tissues with anti-VEGF antibody. Red arrows indicate the tumour. (e) TEM and HRTEM images of the

synthesized Au–Cu_9S_5 NPs. (f) Scheme of a dual plasmonic hybrid nanosystem Au–Cu_9S_5 to enhanced near-field photothermal transduction due to LSPR and application for CT imaging and robust photothermal therapy. (g) Schematic diagram of the PLGA nanostructures encapsulating both $NaGdF_4$:Nd^{3+} nanoparticles and PbS/CdS/ZnS quantum dots. Thermal sensitivities and spectral operating ranges of materials in visible, NIR-I and NIR-II regions. Evolution of the emission intensity of the hybrid nanostructures injected in chicken breast tissue during a heating/cooling cycle of the tissue. Temperature evolution of the tissue during the heating/cooling cycle. The temperatures have been calculated based on the ratio of the of the emission intensity of the $NaGdF_4$:Nd^{3+} nanoparticles and PbS/CdS/ZnS quantum dots. (h) Schematic illustration of multi-branched gold nanoechinus for NIR light activated dual modal photodynamic and photothermal therapy in the second biological window. (i) and (j) UV/Vis/NIR absorption spectrum (black solid line) and excitation spectrum (black dashed line) for singlet oxygen phosphorescence of lipid-coated Au NEs (λ_{em} = 1267 nm). (k) Relative tumour volumes in different treatment and representative mice images showing the sizes of tumours (highlighted by dashed white circles) at day 14th under NIR II.

(a): Reprinted (adapted) with permission from ref.[35], Copyright 2017, American Chemical Society.

(b)-(d): Reprinted (adapted) with permission from ref.[38] Copyright 2015, Wiley-VCH Verlag GmbH & Co. KGaA..

(e)-(f): Reprinted (adapted) with permission from ref.[42], Copyright 2014, American Chemical Society.

(g): Reprinted (adapted) with permission from ref.[46], Copyright 2015, Wiley-VCH Verlag GmbH & Co. KGaA..

(h)-(k): Reprinted (adapted) with permission from ref.[47], Copyright 2014, Wiley-VCH Verlag GmbH & Co. KGaA..

5. NIR-II based treatment and theranostics

As many types of imaging techniques can be combined with NIR-II as described above, numerous developments focused on the integration of diagnosis and therapy have also been pursued. By incorporating a variety of techniques, theranostics has shown promise to provide effective targeted therapies and enhance treatment efficacy. As a newly rising optical imaging technique, NIR-II imaging demonstrates high promise to diagnose diseases and monitor disease development, guide surgery, and evaluate treatment efficacy. Furthermore, NIR-II has also been explored for combination with treatment modalities to achieve diseases theranostics.

5.1 Photothermal therapy guided by NIR-II (PTT/NIR-II)

PTT employs photoabsorbers to generate heat result in growth limitation for cancer cells upon NIR laser irradiation. Compared to traditional therapeutic modalities, PTT possesses the excellent performance of not only high specificity but also precise spatial-temporal selectivity. The efficacy of PTT largely depends on the ability of the photothermal agent to transform light into sufficient heat. Single NIR-II imaging, or multimodal imaging based on NIR-II, can provide real-time PTT guidance for better therapeutic planning before and during PTT. In addition, the targeting NIR-II fluorophores also treat disease with high specificity and high sensitivity. Imaging can minimize side effects by allowing specific irradiation of the tumour and improve therapeutic efficacy by allowing the irradiation time to be optimized.

SPNPs are promising candidates for use as NIR-II absorbing materials. Increasing the π-conjugation length by designing quinoid-stabilized D-A polymers is an effective

strategy for reducing bandgap and provides a beneficial bathochromic shift of absorption to the NIR-II window. Recently, a narrow bandgap D-A conjugated polymer with thiophene-fused benzodifurandione-based oligo (p-phenylenevinylene) as the acceptor and 2,2′-bithiophene as the donor (TBDOPV-DT) has been synthesized and exploited as a solution-processable NIR-II (peak at 1102 nm) photothermal material.[41] TBDOPV-DT has a high extinction coefficient up to 62.57 L^{-1} g^{-1} cm^{-1} at a wavelength of 1102 nm, which enables high photon utilization efficiency in the NIR-II window. This novel NIR-II absorption theranostics probe also demonstrates photothermal conversion efficiency as high as 50.5%, with a low power of 0.45 W at 1102 nm excitation. The high performance photothermal conversion can be extended to photothermal electrical and photothermal mechanical conversions for more convenient use in biological systems or for remote manipulation.

Stoichiometric semiconductor metal sulphide QDs, such as Ag_2S nanocrystals, are not only used for NR-II fluorescence imaging but also promising in PTT, because of their excellent NIR absorbance and high photo-thermal conversion efficiency. For example, hollow nanocage multifunctional Ag_2S nanodots are synthesized by precisely controlled crystal growth in the presence of human serum albumin.[37] Ag_2S nanodots exhibit size-dependent temperature elevations and have high photothermal conversion efficiencies of 33.7–35.0%, which are comparable with those of most other photothermal nanoparticles, such as Au nanorods (up to 22.8%) and ICG-loaded micelles (up to 25.2%). Ag_2S nanodots also produce remarkable fluorescence in the NIR-II region, distinct photoacoustic signals under irradiation with single wavelength NIR light, thereby generating sufficient *in vivo* NIR-II fluorescence and PA signals, as well as hyperthermia at tumours.

To improve NIR-II absorbance and photothermal transduction efficiency, a dual plasmonic hybrid system, Au-Cu_9S_5 NP, has been developed and investigated (Fig. 4e-f).[42] The localized surface plasmon resonance (LSPR) of Cu_9S_5 contributed to the NIR-II absorption cross section by 50% and photothermal transduction efficiency is as high as 37%. This study can improve future chemical design and optimization of NIR-II absorbers and photothermal heaters utilizing SPR enhancement phenomena for a broad range of applications. However, high dose of Cu and Ag may not biotoxicity *in vivo* applications. Besides these Cu-based nanomaterials with inherent LSPRs, there are, however, very few other types of inorganic semiconductor nanomaterials that have strong LSPRs. Therefore, it is a challenge to design and develop heavy metal-free semiconductor photothermal nanomaterials.

Titanium is a transition metal element that has been used as a key constituent of metal alloys in implantable medical devices. When exposed to UV light or radioluminescence, TiO_2 nanoparticles can produce cytotoxic hydroxyl and superoxide radicals for eradicating cancer cells through photodynamic therapy (PDT). Many efforts have been made to extend the photoabsorption range of TiO_2 from the UV to visible-NIR region. Strategies have included preparation of TiO_2 nanoparticles with defects, using doping and/or surface modification by hydrogenation, arc-melting or pulsed laser irradiation. Recently, NIR-II Nb-doped TiO_2 nanocrystals have been synthesized by methanol-assisted thermal decomposition.[43] Compared with white

TiO_2, blue Nb-doped TiO_2 nanocrystals show an intense NIR-II absorption band (1064 nm), high photothermal conversion efficiency (up to 40.6%) and excellent stability. Cancer cells can be thermally ablated under irradiation with a 1064 nm laser, resulting in the elimination of tumours and longer lifespans in mice. This new finding provides insights into the tuning of other wide-bandgap semiconductors without NIR absorption to ones with a strong photothermal effect.

Two-dimensional (2D) nanomaterials have attracted great attention in the past decade because of their ultrathin structure and fascinating physiochemical properties. However, current studies of 2D materials are mainly focused on the PTT in NIR-I window, and very few relevant reports regarding the photothermal effect of 2D nanomaterials in the NIR-II window. Inspired by the great potential of the 2D nanomaterial for biomedical applications, a novel ultrathin 2D niobium carbide (Nb_2C) as a novel phototherapeutic agent, for highly efficient *in vivo* photothermal ablation of mouse tumour xenografts at both NIR-I and NIR-II windows.[44] This ultrathin, lateral-nanosized Nb_2C NSs exhibit extraordinarily high photothermal conversion efficiency (36.4% at NIR-I and 45.65% at NIR-II), as well as high photothermal stability. In addition, another 2D-nanoplatform based on Cu_2MnS_2 nanoplates (NPs) for MRI/multispectral optoacoustic tomography (MSOT) dual-modal imaging-guided PTT of cancer in the NIR-II window have been developed using a facile and effective solvothermal method recently.[45] The Cu_2MnS_2 NPs exhibit low cytotoxicity as well as high photothermal conversion efficiency (~49.38%) and outstanding photostability. Together with the good T1-shortening effect and strong absorbance in the NIR-I and NIR-II region, the Cu_2MnS_2 NPs display high-contrast imaging performance both in MRI and MSOT (900 nm laser source). Moreover, the Cu_2MnS_2 NPs possess excellent PTT efficiency with a low power density (0.6 W cm^{-2}) under 1064 nm laser irradiation. By rationally designing their compositions and exploring related physiochemical properties, these studies provide new perspective for broadening the applications of 2D materials on phototherapy of cancer.

The process of hyperthermia at single cell level is very difficult to control. Intracellular thermal sensing provides an innovative way to investigate the nanostructured systems capable of high-resolution. A new thermal sensing structure, which is a combination of Nd (III)-doped $NaGdF_4$ dielectric RENPs and semiconductor PbS/CdS/ZnS QDs, stabilized by poly(lactic-co-glycolic acid) (PLGA), has recently been reported (Fig. 4g).[46] The NIR-II emission intensity of these hybrid nanostructures from 1000 to 1400 nm is strongly temperature dependent at 1220 nm but not dependent at 1060 nm. The coexistence of these two NIR-II luminescence bands makes them excellent ratiometric thermal sensors. The unique NIR-II thermal sensitivity (~2.5×10^{-2} $°C^{-1}$) of the hybrid nanostructures demonstrates an order of magnitude than that of nanothermometers utilized in NIR-I region.

5.2 NIR-II based photodynamic therapy (PDT/NIR-II)

PDT is a phototherapy that uses light and a photosensitizing chemical substance to treat abnormalities. Light, photosensitizer, and oxygen are three key components in a typical PDT process. Photosensitizer can produce reactive oxygen species (ROS)

under the appropriate light excitation, such as singlet oxygen free radicals or peroxides, leading to irreversible anti-oxidative treatment of cancer cell or inflammation. PDT treatment happens only under light irradiation, which is generally localized in a small area. Clinical treatment using PDT is currently limited to surface tumours since most organic photosensitizers are only activated by UV or visible light, which has high photon energy but very short tissue penetration depths. By now, very rare nanomaterial is able to be sensitized in the formation of singlet oxygen or ROS and to exert PDT effects in the second biological window (1000–1700 nm). Because most of the excited state of NIR-II do not have enough energy to produce singlet oxygen. However, recent study reported that the morphology of the sensitizers and the plasmonic nanomaterials may play a significant role in formation of singlet oxygen and ROS. The Schematic illustration of PDT process using NIR-II light is shown in Scheme 3a.

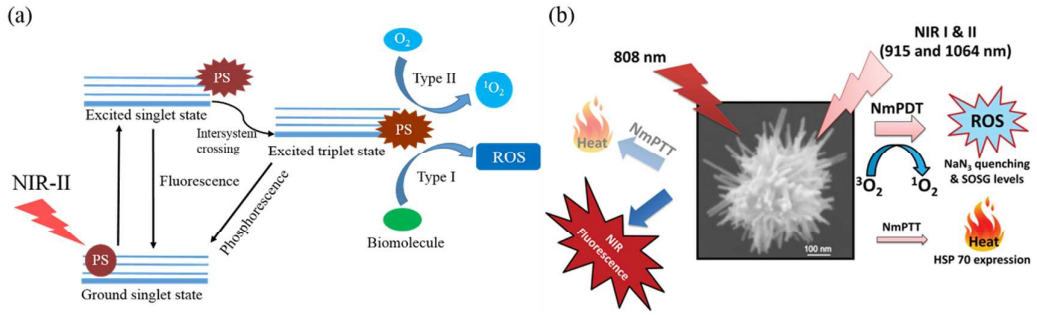

Scheme 3. Schematic illustration of PDT process using NIR-II light. (a) Type I and Type II mechanism reactions in PDT using NIR-II light. Following NIR-II light absorption, the PS reaches an excited singlet state. After an intersystem crossing, the PS, now in a triplet excited state, can react in two ways: react with biomolecules through a hydrogen atom (electron) transfer to form radicals, which react with molecular oxygen to generate ROS (type I reaction); or, the PS in its triplet state can react directly with oxygen through energy transfer, generating singlet oxygen (Type II reaction). PS: photosensitizer; ROS: reactive oxygen species; $^1O_2$: singlet oxygen. (b) Schematic representation of the working mechanisms of NIR light induced fluorescence emission as well as phototherapeutic effects exerted by gold nanoechinus.[47]

For example, a novel gold nanoechinus with a high extinction coefficient (12 $M^{-1}cm^{-1}$) in the NIR region (800–1700 nm) were developed, which is about 7–9 fold higher than traditional organic dyes and 3–4 fold higher than traditional gold nanoparticles or nanorods. This novel nanoagent could also be used as a PTT and PDT dual modal simultaneously for treatment tumours using NIR-I (915 nm) and NIR-II (1064 nm) as shown in Scheme 3b. Moreover, as an effective NIR-II photosensitizer, it has great potential to monitor and destroy the tumours in deep tissue *in vivo* (up to 1 cm) (Fig. 4h-k).[47] Inspired by this result, transition metal oxide semiconductor nanomaterials oxygen-deficient molybdenum oxide nanoparticles with localized surface plasmon resonance are synthesized. Exposure to 1064 nm irradiation can not only effectively convert light into heat but also sensitize the formation of ROS, which exert dramatic cancer cell death and suppression in vivo due to the synergic effect of PTT and PDT.[48] In general, the mechanisms of ROS production of

plasmonic nanomaterials under NIR irradiation are very complicated. It has been reported that one of the plasmon-activated pathways proceeds mainly via an indirect photothermal process for plasmonic nanomaterials under NIR laser irradiation that induces extreme heat development leading to particle fragmentation and increased thermionic electron emission. The higher temperature of the NPs solution under the 1064 nm irradiation may be the main reason for the clear $^1O_2$ production. The detailed mechanism for such an NIR-II excitation wavelength dependent ROS production still requires further study in the future.

5.3 Intraoperative surgical guided by NIR-II imaging

In clinical surgical oncology, delineating tumour margin is very important for precise resecting of tumours. MRI and CT have a considerable role in guiding intraoperative resection plan. However, these systems are very expensive, complex and cannot be easily used during the surgical procedure. Currently, optesthesia and touching remain the dominant ways to decide which parts should be resected or preserved. Optical molecular imaging is a promising technique with high sensitivity in identification of tumour margins. Compared with other imaging modalities, fluorescence imaging offers real-time imaging, superior resolution and high sensitivity and specificity for very small tumour. However, current widely used fluorophores for intraoperative surgery are excited by UV or visible light, which causes photobleaching and poor resolution. These fluorophores also have a low penetration depth and is not available to locate deeper tumours. NIR-II imaging enables not only increased spatial resolution, but with cm tissue penetration depth and quick identification of disease in real time for surgery guidance. Furthermore, NIR-II light minimizes the misjudgement for doctors because it is invisible to human eye, and only NIR-II excited area is visible and displayed on the monitor.

In one study, SWCNTs have shown in NIR-II imaging guidance for cancer resection.[34] Many sub-millimeter tumour nodules, at a maximum depth of 1.8 cm, are discovered in NIR-II image-guided system compared with non-image-guided system. Whereas, for large tumours (> 3 mm in diameter), there is no difference with or without using the image guided system, indicating that SWCNTs show superiority to detect small tumours at earlier stages. In addition, NIR-II imaging observes low tissue autofluorescence, which enhances target-to-background ratios and allows detection of small tumour nodules in confined anatomic regions. The NIR-II small molecule based probe H1 and CQS 1000 also demonstrate great potential for NIR-II image-guided surgery for intraoperative resection of tumours in deep tissue.[3, 15] Under NIR-II imaging, SLN can be detected in deep soft tissue successfully. Moreover, the edge of the SLN is easily distinguished, which avoid unnecessary damage of nerves, vessels and tendons.

5.4 NIR-II based drug delivery

Compared with traditional therapeutic agents, controllable drug delivery systems, including polymeric nanoparticles, liposome particles, nanoemulsions and mesoporous silica particles, offer many advantages, such as high loading capacities,

efficient protection of bioactive drugs and high therapeutic indices. A novel type of RENP-based NIR-II fluorescent mesoporous nanocarrier for oral delivery of protein drugs has been reported recently.[49] The fate of the nanocarrier can be tracked and the amount of drug released in different organs can be monitored semi-quantitatively in real time by measuring NIR-II signals using an absorption competition-induced emission bioimaging system. The NIR-II bioimaging results demonstrate that the protein drugs show little leakage in neutral and acidic organs (e.g. stomach and duodenum) but sustained release at alkalic organs (e.g. intestine). The nanocarriers have a prolonged residence time of up to three days in the intestine, with little deposition (< 0.1%) in other organs such as liver, spleen and kidney. The gastrointestinal effective protein-release percentage of the nanocarriers reaches 62% after three days of release, while the activity of the released enzymes from the orally delivered nanocarriers is largely preserved. For NIR-II based orally administered drugs delivery system, it provides new design strategies.

Ag_2S QDs possess appealing features for *in vivo* NIR-II imaging, with a greater tissue penetration depth (up to 1.2 cm), high temporal resolution (up to 50 ms) and high spatial resolution (up to 25 μm). Ag_2S QDs loaded with drugs also demonstrate perfect drug release under NIR-II excitation. For example, a smart Ag_2S QDs nanoplatform (DOX@PEG-Ag_2S) has been obtained by loading the anti-cancer drug doxorubicin (DOX) into polyethylene glycol functionalization Ag_2S QDs (PEG-Ag_2S QDs). The Ag_2S QDs had up to 93 wt.% drug loading capability, long half circulation time in blood (10.3 h) and more than 8.9% ID/g passive tumour-targeting efficiency in living mice.[50]After accumulating in the tumour tissue, drug from PEG-Ag_2S cargoes is rapidly delivery into cancer cells, causing significant tumour inhibition.

NIR-II based agent is one of the promising photo-controlled drug delivery approaches. During the drug delivery, transient or intermittent NIR-II exposure strategies may be more appropriate and could minimize or avoid possible deleterious thermal effects.

6. Advancement of NIR-II imaging system.

NIR-II imaging system is an image capture setup that acquires NIR-II emission signals from NIR-II fluorophores. NIR-II fluorescence imaging system development has to be in sync with the NIR-II fluorophores development to fully realize the power of NIR-II imaging, and such systems promote the broad applications of NIR-II fluorophores in pre-clinical research and for future clinical translation. Unlike the conventional imaging modalities such as MRI and CT, NIR-II fluorescence imaging systems are more versatile and possess advantages of real time imaging capability (rapid video-frame rate visual feedback, up to 30 frames per second) and absence of high energy and ionizing radiation, and they can even be potentially constructed as portable imaging systems.

The emergence of NIR-II detectors (e.g., indium gallium arsenide, InGaAs detectors) that suitable in the region of 1000- 1700 nm makes it is possible to develop NIR-II fluorescence imaging systems. Current NIR-II imaging systems are mostly constructed in-house using original equipment manufacturer components such as a

continuous wave NIR laser and an NIR camera together with suitable filters, focusing lenses and collimators that depend on the optical characteristics of the complementary NIR-II fluorophores. Briefly, the InGaAs camera is placed at a fixed distance away from the platform; lenses and filters are placed between the camera and platform, where the image magnification is adjusted by changing the lens sets and filters; a xenon flashlight is used to resolve the animal location, and the excitation source is collimated to provide a uniform and constant excitation beam radius.

Currently, there are two basic types of NIR-II imaging systems that have been reported (see Fig. 5a and b). The main differences of these two systems focus on the different approaches adopted to minimize the thermal influence of the NIR excitation source. In the system reported by Moghe's group,[5] the collimated excitation source is mounted on a translation stage to enable a slowly scanning across the whole animal's body. The moving excitation source prevents the "overheating" of the animal since the source exposure is limited by setting a rapid scan rate (~10 to 20 mm/sec). In another design reported by Dai's group,[29] the NIR excitation source is kept in one fixed position. With suitable selection of appropriate lenses, full body imaging is achieved for a desired magnification. In this setup, a computer-controlled shutter is incorporated to reduce the thermal effects. The lenses and objectives between the camera and animal allows for fine adjustment of the position and further magnification of interesting region. In further development, an in-house stereotactic animal platform fixed on a motorized translational stage allows for digital position adjustments of the mouse. Using small animal NIR-II imaging systems, the high spatial (micrometer resolution) and high temporal (<200 ms per frame) resolution can be achieved at deep depths.

Interestingly, NIR-II imaging setup reported by Moghe's group can acquire the whole animal body imaging rapidly, but it largely depends on brightly emitting NIR-II fluorophores due to the shorter acquisition time. NIR-II setup reported by Dai's group allows the averaging of multiple images over a smaller area and longer durations, which enable the higher resolution images with a reducing dependency on brightly emitting NIR-II fluorophores.

Moreover, there are also different approaches to reduce the thermal influence on the NIR-II detector. Moghe's group has used a thermoelectric cooled InGaAs camera detector (Sensors Unlimited, Goodrich, Princeton, NJ), whilst Dai's group has used a liquid nitrogen cooled InGaAs camera unit (Princeton Instruments, Princeton, NJ), which is typically more stable with a lower dark count and higher signal-to-noise ratio. Using the liquid nitrogen cooled camera unit also allows the detection of relatively weaker NIR-II emitting signals.

Despite recent advancements in NIR-II fluorescence systems are achieved, a multi-modal imaging approach would enable more accurate diagnosis with potentially a reduction of false positives or negatives. However, integrating two or more imaging systems into one device platform remains a challenge. The difficulties of designing multi-modal imaging systems arise from hardware incompatibilities and the distinctly different imaging principles of diverse imaging modalities that lead to different image acquisition time scales between each imaging modality.

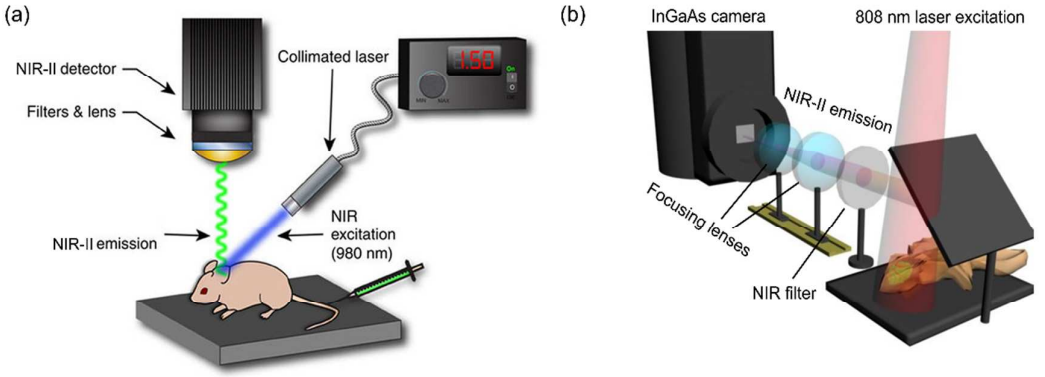

Figure 5. Schematics of NIR-II imaging systems. (a) The NIR-II imaging system reported by Moghe's group mainly consists of a fiber-coupled NIR laser photodiode, and a thermoelectric cooled InGaAs camera with appropriate filter sets. (b) The NIR-II imaging system reported by Dai's group mainly consists of a liquid-nitrogen-cooled InGaAs camera, diode laser coupled to a 4.5 mm focal length collimator with accompanying appropriate filter sets and objectives based on the preferred magnification.

(a): Reprinted (adapted) with permission from ref.[5], Copyright 2013, Nature Publishing Group.

(b): Reprinted (adapted) with permission from ref.[29], Copyright 2014, Nature Publishing Group.

7. Perspective

Until now, varieties of NIR-II fluorophores, ranging from small molecules dyes, to small molecule protein complexes, to small molecules encapsulated organic nanoparticles, to D-A copolymers, to inorganic particles (QDs, RENPs, SWCNTs), have been designed and synthesized. During the development of NIR-II fluorophores and NIR-II based multimodal imaging and theranostics, several key points should be noted.

1). Clinical translation of NIR-II imaging: Besides applications in the pre-clinical research and in vitro assays, it is paramount to translate NIR-II imaging techniques into clinic. Importantly, conventional NIR-I dye ICG has been demonstrated to be capable for NIR-II imaging, which makes quick clinical translation of NIR-II imaging highly feasible. However, ICG may suffers some limitations. First, the tailed portion of the emission spectrum of ICG is used for NIR-II imaging and thus the efficiency of the photon usage is not high. Second, ICG has no targeting specificity and the clinical indications approved by FDA are rather limited. Third, the photostability of ICG is not high. Fourth, the in vivo pharmacokinetics of ICG is not ideal for many applications. All these problems urge the continue synthesis of other novel small molecule NIR-II dyes for clinical broad use.

2). Aim at synthesis of new NIR-II fluorophores: high quantum yield and photostability, non-biotoxicity, and functionalizability are the first several important criterions to be considered for designing new generation of NIR-II fluorophores. In addition, direct chemical design of NIR-II fluorophores with targeting functions, rather than post-synthesis surface-targeting modifications, is more effective to improve therapeutic efficacy. The chemical design and synthesis of biodegradable NIR-II fluorophores, with rationally controlled degradation rates, should also be encouraged. Among the recent developed NIR-II fluorophores, the small molecule

dyes, based organic nanoparticles and complex have promising translational potential from small-animal studies into clinic uses. However, as the biological use of these NIR-II fluorophores are reported only recently and further improvement are required including improving their quantum yields, molar attenuation coefficient as well as synthesis process according to the FDA's current GMP regulations.

3). Aim at NIR-II based multimodal imaging: Considering PET can be used in pre-operative imaging and NIR-II can be used in intra-operative real-time imaging in high resolution, PET/NIR-II imaging will likely bring high impact to the patient imaging and image-guided therapy. It would be important to test the advantages of PET/NIR-II dual modal probes in clinic. In addition, it is expected that PAI/NIR-II dual modal imaging will make rapid progress because many dyes can serve as reporters for both PAI and optical imaging. However, the integration of several imaging modalities into one system is a great challenge due to the different hardware and the imaging mechanisms. By now, there are no any reports about NIR-II based more than dual modal imaging systems (e.g. NIR-II/MRI/PET or NIR-II/PET/PAI), but such modal imaging systems hold high promise to acquire complementary information. For example, with NIR-II/MRI/PET tri-modal imaging system, the high sensitivity and unlimited penetration depth of PET (10−11−10−12 M) can be used for whole body screening to identify regions of interest roughly, then reducing the volume of tissue that needs to scan. MRI has no radiation involved, and high resolution images can be obtained. The NIR-II imaging will provide a real-time imaging and obtain molecular and functional information of the diseases.

4). Aim at NIR-II based treatment and theranostics: It is important to note that most of NIR-II fluorophores show low quantum yields. One important reason is that the absorbed photon energy is likely to be converted into thermal. Thus NIR-II fluorophores are potential sources to enable photothermal therapy. Few NIR-II fluorophores have higher triplet electronic energy levels than the singlet energy level of the oxygen molecule, and it may be great challenge to achieve photodynamic therapy using NIR-II fluorophores. Moreover, it would be important to keep a rational balance between NIR-II emission and non-radiation emission according to different requirements. Doses of NIR-II fluorophores should receive careful consideration in both imaging and therapy. For example, large amounts of NIR-II fluorophores may result in fluorescence quenching but may be useful in enhancing thermal, particular in PTT and PAI applications. In intraoperative NIR-II image guided surgery, it will be helpful to integrate other clinic imaging modalities, such as PET or MRI, which will obtain more information beyond the single NIR-II imaging.

5). Aim at NIR-II imaging system: To benefit from the NIR-II imaging platform, it is very reliant on the understanding of the requirements of each imaging platform and the physical characteristics of the NIR-II fluorophores. Besides, the hardware platforms (scan rate, lenses, collimators, working distance, exposure duration) and software algorithms for signal processing and image acquisition need to be designed to reduce undesired thermal noise often associated with NIR-II imaging and to enhance the signal-to-noise ratio.

On the way to construct novel clinically translatable NIR-II fluorophores, many challenges remain but will be overcome based on the previous success on NIR-II probe development and the use of FDA approved NIR-I dye for NIR-II imaging. It is hoped that these promising multifunctional NIR-II fluorophores leading to multimodal imaging and theranostics will make a significant contribution to human healthcare.

8. Conclusions

In summary, NIR-II imaging as a new rising modality has several advantages over convention NIR-I imaging and other current medical imaging modalities. Significant improvement in imaging resolution and depth can be achieved in NIR-II imaging because of reduced photon scattering and low autofluorescence background at longer wavelengths. NIR-II imaging allows visualize deeper anatomical structures with a much higher clarity that are not feasible with NIR-I imaging. Numerous NIR-II fluorophores, from small organic molecules to organic and inorganic nanoparticles have been successfully development, and their broad biomedical applications such as multimodal imaging, photothermal and photodynamic therapy, guidance for intraoperative surgery, and drug delivery have been demonstrated. The crucial breakthrough of research on NIR-II fluorophores and imaging system over the past decade highlights the great impact of this technique to basic research and potentially clinical theranostics of diseases.

Acknowledgements

This work was partially supported by the Office of Science (BER), US Department of Energy (DE-SC0008397); the National Natural Science Foundation of China (61775145, 31771584, 61605124, 61620106016, 61525503, 81727804, 61605130 and 51602201); Guangdong Natural Science Foundation Innovation Team (2014A030312008); the National Basic Research Program of China (Grant 2015CB352005); Hong Kong, Macao, and Taiwan cooperation innovation platform & major projects of international cooperation in Colleges and Universities in Guangdong Province (2015KGJHZ002); Shenzhen Basic Research Project (JCYJ20170412110212234, JCYJ20160308093035903, JCYJ20150930104948169, JCYJ20160328144746940, GJHZ20160226202139185).

References

1. A. B. Eva Hemmer, François Légaréa and Fiorenzo Vetrone, *Nanoscale Horizon*, 2016, **1**, 168-184.
2. G. Hong, A. L. Antaris and H. Dai, *Nature Biomedical Engineering*, 2017, **1**, 0010.
3. K. Shou, C. Qu, Y. Sun, H. Chen, S. Chen, L. Zhang, H. Xu, X. Hong, A. Yu and Z. Cheng, *Advanced Functional Materials*, 2017, **27**, 1700995.
4. A. L. Antaris, H. Chen, K. Cheng, Y. Sun, G. Hong, C. Qu, S. Diao, Z. Deng, X. Hu, B. Zhang, X. Zhang, O. K. Yaghi, Z. R. Alamparambil, X. Hong, Z. Cheng and H. Dai, *Nature Materials*, 2015, **15**, 235-242.

5. D. J. Naczynski, M. C. Tan, M. Zevon, B. Wall, J. Kohl, A. Kulesa, S. Chen, C. M. Roth, R. E. Riman and P. V. Moghe, *Nature Communications*, 2013, **4**, 1-10.
6. K. Welsher, Z. Liu, S. P. Sherlock, J. T. Robinson, Z. Chen, D. Daranciang and H. Dai, *Nat Nano*, 2009, **4**, 773-780.
7. Z. Starosolski, R. Bhavane, K. B. Ghaghada, S. A. Vasudevan, A. Kaay and A. Annapragada, *PLOS ONE*, 2017, **12**, e0187563.
8. J. A. Carr, D. Franke, J. R. Caram, C. F. Perkinson, V. Askoxylakis, M. Datta, D. Fukumura, R. K. Jain, M. G. Bawendi and O. T. Bruns, *bioRxiv*, 2017,DOI: 10.1101/100768
9. A. L. Antaris, H. Chen, S. Diao, Z. Ma, Z. Zhang, S. Zhu, J. Wang, A. X. Lozano, Q. Fan, L. Chew, M. Zhu, K. Cheng, X. Hong, H. Dai and Z. Cheng, *Nature Communications*, 2017, **8**, 15269.
10. Y. Sun, C. Qu, H. Chen, M. He, C. Tang, K. Shou, S. Hong, M. Yang, Y. Jiang, B. Ding, Y. Xiao, L. Xing, X. Hong and Z. Cheng, *Chemical Science*, 2016, **7**, 6203-6207.
11. Y. Sun, X. Zeng, Y. Xiao, C. Liu, H. Zhu, H. Zhou, Z. Chen, F. Xu, J. Wang, M. Zhu, J. Wu, M. Tian, H. Zhang, Z. Deng, Z. Cheng and X. Hong, *Chemical Science*, 2018, DOI: 10.1039/C7SC04774F
12. X.-D. Zhang, H. Wang, A. L. Antaris, L. Li, S. Diao, R. Ma, A. Nguyen, G. Hong, Z. Ma, J. Wang, S. Zhu, J. M. Castellano, T. Wyss-Coray, Y. Liang, J. Luo and H. Dai, *Advanced Materials*, 2016, **28**, 6872-6879.
13. S. Zhu, Q. Yang, A. L. Antaris, J. Yue, Z. Ma, H. Wang, W. Huang, H. Wan, J. Wang, S. Diao, B. Zhang, X. Li, Y. Zhong, K. Yu, G. Hong, J. Luo, Y. Liang and H. Dai, *Proceedings of the National Academy of Sciences*, 2017, **114**, 962-967.
14. Y. Feng, S. Zhu, A. L. Antaris, H. Chen, Y. Xiao, X. Lu, L. Jiang, S. Diao, K. Yu, Y. Wang, S. Herraiz, J. Yue, X. Hong, G. Hong, Z. Cheng, H. Dai and A. J. Hsueh, *Chemical Science*, 2017, **8**, 3703-3711.
15. Y. Sun, M. Ding, X. Zeng, Y. Xiao, H. Wu, H. Zhou, B. Ding, C. Qu, W. Hou, A. G. A. Er-bu, Y. Zhang, Z. Cheng and X. Hong, *Chemical Science*, 2017, **8**, 3489-3493.
16. Z. Tao, G. Hong, C. Shinji, C. Chen, S. Diao, A. L. Antaris, B. Zhang, Y. Zou and H. Dai, *Angewandte Chemie International Edition*, 2013, **52**, 13002-13006.
17. G. Hong, Y. Zou, A. L. Antaris, S. Diao, D. Wu, K. Cheng, X. Zhang, C. Chen, B. Liu, Y. He, J. Z. Wu, J. Yuan, B. Zhang, Z. Tao, C. Fukunaga and H. Dai, *Nature Communications*, 2014, **5**, 4206.
18. K. Shou, Y. Tang, H. Chen, S. Chen, L. Zhang, A. Zhang, Q. Fan, A. Yu and Z. Cheng, *Chemical Science*, 2018, DOI: 10.1039/C8SC00206A
19. G. Hong, J. T. Robinson, Y. Zhang, S. Diao, A. L. Antaris, Q. Wang and H. Dai, *Angewandte Chemie International Edition*, 2012, **124**, 9956-9959.
20. C. Li, Y. Zhang, M. Wang, Y. Zhang, G. Chen, L. Li, D. Wu and Q. Wang, *Biomaterials*, 2014, **35**, 393-400.
21. G. Chen, F. Tian, Y. Zhang, Y. Zhang, C. Li and Q. Wang, *Advanced Functional Materials*, 2014, **24**, 2481-2488.
22. R. Tang, J. Xue, B. Xu, D. Shen, G. P. Sudlow and S. Achilefu, *ACS Nano*, 2015, **9**, 220-230.
23. M. Kamimura, N. Kanayama, K. Tokuzen, K. Soga and Y. Nagasaki, *Nanoscale*, 2011, **3**, 3705-3713.
24. M. Zevon, V. Ganapathy, H. Kantamneni, M. Mingozzi, P. Kim, D. Adler, Y. Sheng, M. C.

Tan, M. Pierce, R. E. Riman, C. M. Roth and P. V. Moghe, *Small*, 2015, **11**, 6347-6357.
25. W. Shao, G. Chen, A. Kuzmin, H. L. Kutscher, A. Pliss, T. Y. Ohulchanskyy and P. N. Prasad, *Journal of the American Chemical Society*, 2016, **138**, 16192-16195.
26. J. T. Robinson, G. Hong, Y. Liang, B. Zhang, O. K. Yaghi and H. Dai, *Journal of the American Chemical Society*, 2012, **134**, 10664-10669.
27. K. Welsher, S. P. Sherlock and H. Dai, *Proceedings of the National Academy of Sciences*, 2011, **108**, 8943-8948.
28. G. Hong, J. C. Lee, J. T. Robinson, U. Raaz, L. Xie, N. F. Huang, J. P. Cooke and H. Dai, *Nature medicine*, 2012, **18**, 1841-1846.
29. G. Hong, S. Diao, J. Chang, A. L. Antaris, C. Chen, B. Zhang, S. Zhao, D. N. Atochin, P. L. Huang, K. I. Andreasson, C. J. Kuo and H. Dai, *Nature Photonics*, 2014, **8**, 723-730.
30. Y. Yomogida, T. Tanaka, M. Zhang, M. Yudasaka, X. Wei and H. Kataura, *Nature Communications,* 2016, **7**, 12056.
31. S. Diao, J. L. Blackburn, G. Hong, A. L. Antaris, J. Chang, J. Z. Wu, B. Zhang, K. Cheng, C. J. Kuo and H. Dai, *Angewandte Chemie International Edition*, 2015, **54**, 14758-14762.
32. N. M. Iverson, P. W. Barone, M. Shandell, L. J. Trudel, S. Sen, F. Sen, V. Ivanov, E. Atolia, E. Farias, T. P. McNicholas, N. Reuel, N. M. A. Parry, G. N. Wogan and M. S. Strano, *Nature Nanotechnology*, 2013, **8**, 873-880.
33. D. J. Naczynski, C. Sun, S. Türkcan, C. Jenkins, A. L. Koh, D. Ikeda, G. Pratx and L. Xing, *Nano Letters*, 2015, **15**, 96-102.
34. D. Ghosh, A. F. Bagley, Y. J. Na, M. J. Birrer, S. N. Bhatia and A. M. Belcher, *Proceedings of the National Academy of Sciences*, 2014, **111**, 13948-13953.
35. K. Cheng, H. Chen, C. H. Jenkins, G. Zhang, W. Zhao, Z. Zhang, F. Han, J. Fung, M. Yang, Y. Jiang, L. Xing and Z. Cheng, *ACS Nano*, 2017, **11,** 12276–12291
36. Y. Sheng, L.-D. Liao, A. Bandla, Y.-H. Liu, N. Thakor and M. C. Tan, *ACS Biomaterials Science & Engineering*, 2016, **2**, 809-817.
37. T. Yang, Y. a. Tang, L. Liu, X. Lv, Q. Wang, H. Ke, Y. Deng, H. Yang, X. Yang, G. Liu, Y. Zhao and H. Chen, *ACS Nano*, 2017, **11**, 1848-1857.
38. C. Li, L. Cao, Y. Zhang, P. Yi, M. Wang, B. Tan, Z. Deng, D. Wu and Q. Wang, *Small*, 2015, **11**, 4517-4525.
39. J. H. Choi, F. T. Nguyen, P. W. Barone, D. A. Heller, A. E. Moll, D. Patel, S. A. Boppart and M. S. Strano, *Nano Letters*, 2007, **7**, 861-867.
40. C. Wu, Y. Zhang, Z. Li, C. Li and Q. Wang, *Nanoscale*, 2016, **8**, 12531-12539.
41. Y. Cao, J.-H. Dou, N.-j. Zhao, S. Zhang, Y.-Q. Zheng, J.-P. Zhang, J.-Y. Wang, J. Pei and Y. Wang, *Chemistry of Materials*, 2017, **29**, 718-725.
42. X. Ding, C. H. Liow, M. Zhang, R. Huang, C. Li, H. Shen, M. Liu, Y. Zou, N. Gao, Z. Zhang, Y. Li, Q. Wang, S. Li and J. Jiang, *Journal of the American Chemical Society*, 2014, **136**, 15684-15693.
43. N. Yu, Y. Hu, X. Wang, G. Liu, Z. Wang, Z. Liu, Q. Tian, M. Zhu, X. Shi and Z. Chen, *Nanoscale*, 2017, **9**, 9148-9159.
44. H. Lin, S. Gao, C. Dai, Y. Chen and J. Shi, *Journal of the American Chemical Society*, 2017, **139**, 16235-16247.
45. K. Ke, W. Yang, X. Xie, R. Liu, L.-L. Wang, W.-W. Lin, G. Huang, C.-H. Lu and H.-H. Yang, *Theranostics*, 2017, **7**, 4763-4776.

46. E. N. Cerón, D. H. Ortgies, B. del Rosal, F. Ren, A. Benayas, F. Vetrone, D. Ma, F. Sanz-Rodríguez, J. G. Solé, D. Jaque and E. M. Rodríguez, *Advanced Materials*, 2015, **27**, 4781-4787.
47. P. Vijayaraghavan, C.-H. Liu, R. Vankayala, C.-S. Chiang and K. C. Hwang, *Advanced Materials*, 2014, **26**, 6689-6695.
48. W.Yin, T. Bao, X. Zhang, Q. Gao, J. Yu, X. Dong, L. Yan, Z. Gu and Y. Zhao, *Nanoscale*, 2018, **10**, 1517-1531.
49. R. Wang, L. Zhou, W. Wang, X. Li and F. Zhang, *Nature Communications*, 2017, **8**, 14702.
50. F. Hu, C. Li, Y. Zhang, M. Wang, D. Wu and Q. Wang, *Nano Research.*, 2015, **8**, 1637-1647.

Graphical Abstract

Crucial Breakthrough of Second Near-infrared Biological Window Fluorophores: Design and Synthesis toward Multimodal Imaging and Theranostics

Shuqing He,[a,b] Jun Song,*[a] Junle Qu,*[a] and Zhen Cheng*[b]

* To whom correspondence should be addressed.

[a] Key Laboratory of Optoelectronic Devices and Systems of Ministry of Education and Guangdong Province, College of Optoelectronic Engineering, Shenzhen University, Shenzhen, Guangdong 518060, China
E-mail: songjun@szu.edu.cn jlqu@szu.edu.cn

[b] Molecular Imaging Program at Stanford (MIPS), Bio-X Program, and Department of Radiology, Canary Center at Stanford for Cancer Early Detection,
Stanford University, Stanford, California 94305-5344, USA.
E-mail: zcheng@stanford.edu

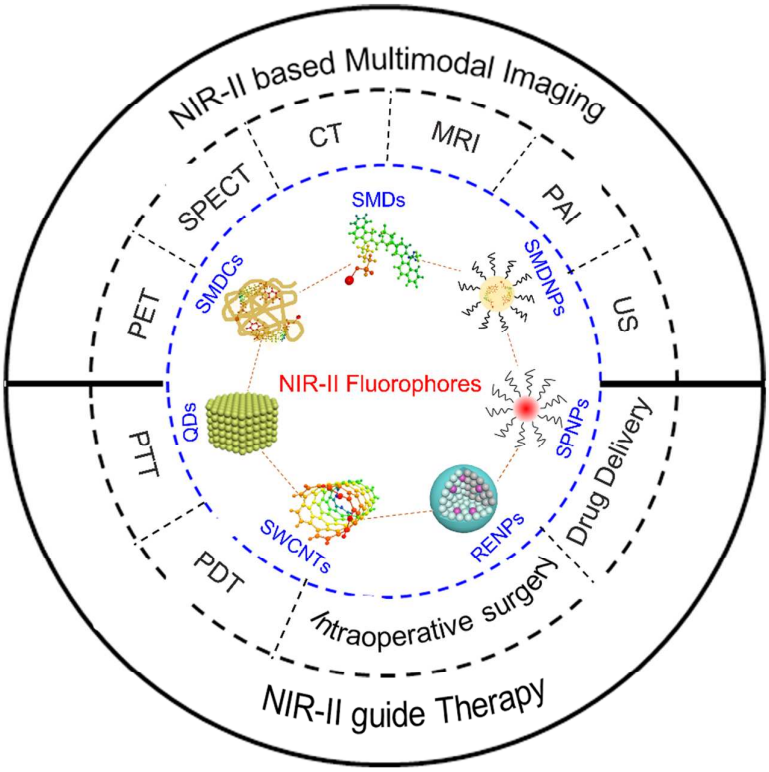

Graphical Abstract Caption: Recent advancements in the chemical design and synthesis of fluorophores in the second near-infrared biological window (NIR-II) for multimodal imaging and theranostics are summarized and highlighted in the review article.